Journal of Drug Delivery Science and Technology 121 (2026) 108370

Contents lists available at ScienceDirect

Journal of Drug Delivery Science and Technology

journal homepage: www.elsevier.com/locate/jddst

PEG/chitosan-functionalized thymol-loaded span-based nanovesicles for enhanced Alzheimer's therapy: *In-Vivo* evaluation in induced rat model

Shaimaa A. Mohamed [a], Eman Gomaa [b,c], Hanaa A. Elghamry [b], Esraa M. Fahmy [d], Asmaa I. Abdelaty [e], Mohamed A. Megahed [a,f,*]

[a] Department of Pharmaceutics and Pharmaceutical Technology, Faculty of Pharmacy, Egyptian Russian University, P.O. Box 11829, Badr city, Cairo, Egypt
[b] Department of Pharmaceutics, Faculty of Pharmacy, Zagazig University, Zagazig, 44519, Egypt
[c] Nanotechnology Research Center (NTRC), The British University in Egypt (BUE), Cairo, 11837, Egypt
[d] Department of Pharmacology, Faculty of Veterinary Medicine, Zagazig University, Zagazig, 44519, Egypt
[e] Department of Behavior and Management of Animal, Poultry and Aquatics, Faculty of Veterinary Medicine, Zagazig University, Zagazig, 44519, Egypt
[f] Department of Pharmaceutics, Faculty of Pharmacy, Balagrae University, Benghazi, Libya

ARTICLE INFO

Keywords:
Niosomes
Thymol
Alzheimer's disease
Box-Behnken design
Chitosan
Polyethylene glycol
In-vivo study

ABSTRACT

The practical relevance of Thymol (THYM), one of the traditional neuroprotective phytotherapy for Alzheimer's disease (AD), has significant difficulties because of its low oral absorption and difficulty in passing BBB. To improve its efficacy and penetrability to brain, span-based nanocarriers, niosomes (NIO), were fabricated and optimized using Box-Behnken design. Three variables' effects were evaluated: HLB value of span, cholesterol molar ratio and drug concentration. The optimized formula (OF) was prepared, examined for particle size (PS), zeta potential (ZP), and entrapment efficiency (EE) and scored 296.85 ± 1.59 nm, -41.66 ± 2.85 mV and 81.00 ± 1.63%, respectively. Optimized THYM-NIO was further surface modified by PEG/chitosan polymers to improve its targetability and efficacy for delivering THYM to brain. Modified OF formulae, PEGylated THYM-NIO (P-OF), THYM-chitosomes (CH-OF) and PEGylated THYM-chitosomes (PCH-OF), were then characterized by measuring PS, ZP, and EE% and showed excellent stability upon storage for 3 months. In vivo pharmacodynamic study was applied on $AlCl_3$ induced Alzheimer's rat model to evaluate the efficacy of coated formulae versus uncoated OF and free THYM. Improvement of THYM brain delivery through coated and uncoated formulae was validated by enhanced cognitive functions approved by behavior tests and significant perfection of oxidative stress biomarkers (MDA, GSH, MOD, and GPx), anti-inflammatory biomarkers (TNF-α, IL-1β) and specific neuronal biomarkers (GFAP, dopamine, and Aβ) with superiority of double-coated formula (PCH-OF). Moreover, histopathological examination strengthened the preference of coated formulae over uncoated THYM-NIO. Development of PEGylated THYM-chitosomes is a promising approach to improve brain targetability and efficacy of THYM for AD management.

1. Introduction

Neurological disorders affecting the central nervous system (CNS) impose a major global health burden, impacting approximately 1.5 billion individuals worldwide [1,2]. Among these conditions, Alzheimer's disease (AD) is the utmost widespread reason of dementia and denotes a chronic, age-related neurodegenerative illness that progresses inexorably and cannot be reversed. The disorder is clinically marked by a gradual decline in memory and cognition, accompanied by behavioral and psychological alterations that profoundly disrupt independent living and overall quality of life [3,4].

From an etiological perspective, fewer than 10% of Alzheimer's cases are attributable to inherited mutations in the amyloid precursor protein (APP) gene or in the presenilin genes PSEN1 and PSEN2 [5,6]. The symptomatic progression of AD is driven by extensive and irreversible neuronal degeneration, together with the deposition of aberrant

* Corresponding author. Department of Pharmaceutics and Pharmaceutical Technology, Faculty of Pharmacy, Egyptian Russian University, Badr city, P.O. Box 11829, Cairo, Egypt.
E-mail addresses: Shaimaaabdelaziz313@gmail.com (S.A. Mohamed), Eman_pharmaceutics@yahoo.com (E. Gomaa), Hanaaelghamry@yahoo.com (H.A. Elghamry), Esraa.fahmy@zu.edu.eg (E.M. Fahmy), asmaaibrahimvet@gmail.com (A.I. Abdelaty), Mohamed_adel@eru.edu.eg, Mohamed.A.A.Megahed@gmail.com, Mohamedadel@ub.edu.ly (M.A. Megahed).

https://doi.org/10.1016/j.jddst.2026.108370
Received 23 January 2026; Received in revised form 12 April 2026; Accepted 23 April 2026
Available online 24 April 2026

extracellular protein aggregates known as amyloid-β (Aβ) plaques, which are widely recognized as a defining neuropathological feature of the disease [7]. In parallel, Alzheimer's pathology is further characterized by the intracellular accumulation of neurofibrillary tangles (NFTs) composed of abnormally hyperphosphorylated tau protein, as well as senile plaque development and pronounced synaptic dysfunction, all of which contribute critically to disease progression [8,9].

Moreover, cholinergic deficiencies have been identified in Alzheimer's disease. Recent evidence links dopaminergic signaling impairments to cognitive and neuropsychiatric changes associated with AD [10]. Accordingly, dopamine is a crucial neurotransmitter for proper thinking and cognitive function. This finding suggests that improving the brain's dopaminergic system might help treat Alzheimer's and other related brain disorders.

Additionally, chronic inflammation is recognized to have a significant part in the diverse etiology of AD. Activated astrocytes producing glial fibrillary acidic protein (GFAP) are intimately connected with Alzheimer's pathology, such as tangles, neurotic plaques, and amyloid deposits [11,12]. Also IL-6 and TNF-α are key mediators of inflammation in AD [13].

Indeed, it has been established that oxidative stress and inflammation are the primary pathogenic processes of AD development [14]. Nevertheless, it remains unclear whether direct oxidative injury causes the development of Aβ [15]. The activities of superoxide dismutase (SOD) and glutathione peroxidase (GPx), along with the levels of malondialdehyde (MDA) and glutathione (GSH), are widely regarded as hallmark features for the assessment of oxidative stress [16]. Anti-inflammatory and antioxidant herbal medications may lower inflammation and oxidative stress in the brain tissue in AD [17].

Thymol (THYM), (5-methyl-2-iso-propylphenol) is gotten from the plant, *Thymus vulgaris L* [17,18]. Monoterpene phenol, which is a key bioactive component in thyme, has demonstrated strong neuroprotective properties. It also demonstrates a range of biological actions, including anti-inflammatory via decreasing cytokine and chemokine recruitment, [19,20], antioxidant properties via chelating metal ions, increasing the body's own enzymatic and non-enzymatic antioxidants, scavenging free radicals [20,21] and improves cognitive functions in a model of dementia [8,22]. Thymol's substantial antioxidant properties may be useful in reducing the progression of different oxidative stress-related disorders [3]. Recent researches have demonstrated that antioxidant-rich diets have a significant role in the protection and prevention of neurodegenerative disorders, including AD [3].

Moreover, it was postulated that thymol has anticholinesterase effect [23–25], antihyperglycemic and hyperlipidemic activities [17,26]. Although thymol holds significant potential for applications in the pharmaceutical and food industries, its use is limited by poor oral bioavailability (16%) [27] and reduced aqueous solubility (1 mg/mL) [28].

Nanotechnology is an effective and acceptable way for improving the physicochemical characteristics of thymol [20]. In this effort, thymol was encapsulated into niosomes to reduce its limits, increase its bioactive potential, and penetration ability to BBB improving its application in the treatment of AD. Niosomes are colloidal systems that are composed of non-ionic synthetic surfactants that may self-assemble into closed bilayer structures that define one or more interior aqueous compartments. Compared to conventional liposomes, niosomes have the potential to provide a number of advantages, including decreased cost, enhanced physicochemical stability, prolonged shelf life, more formulation diversity, and additional sterilizing choices [29,30]. However, the biggest benefit of these revolutionary carriers is undoubtedly the ability of integrating suitable surfactants in their structure, correctly functionalized in order to interact with certain biological targets [29]. It may be possible to create nanocarriers that can facilitate drug transport over the BBB by conjugating ligands that target the BBB on the niosomal surface [31].

Chitosan (CS) is derived by the chemical deacetylation of chitin, a naturally found, biocompatible polysaccharide predominantly sourced from the exoskeletons of crustaceans, including crabs. Its favorable properties are biocompatibility, non-toxicity, non-irritancy, and non-immunogenicity making CS an attractive material for pharmaceutical applications, particularly targeted drug delivery (TDD). Unlike many other natural polymers, CS carries a positive charge and exhibits mucoadhesive characteristics. As a result, CS has been employed in several applications, including topical, ophthalmic, cancer treatment, mucosal, colon-targeted medication delivery, and gene transfer [32,33]. Surface modifications of nanoparticles (NPs) with chitosan give several advantages; prolonged drug release combined with mucoadhesive nature, boosting drug absorption and delayed drug release [34,35].The coating of chitosan reduces burst drug release while increasing penetration and retention of nanovesicles due to the interaction between the negatively charged membrane and positively charged chitosan [34,36]. A recent study highlighted chitosan-decorated drug delivery systems as effective in delivering medications to the brain, because of the mucoadhesive nature of chitosan [37,38].

Polymeric NPs based on (LMW) chitosan are intriguing candidates for the non-invasive transport of medicines via the BBB, because of their multiple benefits, including no toxicity, biodegradability, biocompatibility, and mucoadhesive properties [37,39]. Numerous investigations have explored the use of chitosan-functionalized nanocarriers for the targeted delivery of therapeutic compounds in the management of neurodegenerative and neuropsychiatric disorders, including Alzheimer's disease, Parkinson's disease, gliomas, cerebral ischemia, and schizophrenia. The mucoadhesive properties of chitosan enable electrostatic interactions with the negatively charged glycocalyx and phospholipids of the blood–brain barrier (BBB), thereby facilitating targeted and efficient drug delivery to the central nervous system [38,40,41].

PEGylation of NPs can be a very useful mechanism for boosting therapeutic drug systemic distribution. PEG coatings can be crucial in the design of NPs for drug/gene delivery applications, which will support future research into how PEG coatings' characteristics affect NP biodistribution, brain drug availability, and bodily clearance [42,43]. PEGylated NPs are effectively beneficial in the treatment of brain diseases specially with a compromised BBB than equivalent uncoated NPs [44–46]. Beyond the advantages for targeted drug delivery, PEGylation of nanoparticles offers several additional benefits: (i) it enhances particle dispersibility, (ii) prevents nanoparticle aggregation and premature clearance, (iii) reduces opsonin protein binding and limits macrophage-mediated uptake, and (iv) prolongs systemic circulation time [47]. Pharmacokinetic enhancement and improved therapeutic performance have been reported for PEG-based micellar systems, where PEGylation significantly increased systemic stability and drug bioavailability [48].

Additionally, modulating the surface charge of nanoparticles by incorporating cationic or anionic surfactants can improve cellular uptake and strengthen interactions with biological membranes [49,50]. These surface functionalization techniques present potential opportunities for improving the therapeutic effectiveness of THYM-loaded NPs. Recent advances in nanomedicine have highlighted multifunctional nanosystems capable of integrating targeting capacity with inflammation modulation, thereby enhancing therapeutic outcomes [51,52].In this context, the present study aims to encapsulate THYM in optimized nanosized niosomes, combined with surface functionalization using PEG and CS coatings, to enhance its therapeutic efficacy against AD while achieving a sustained drug release profile.

2. Materials and methods

2.1. Materials

THYM, polyethylene glycol 4000 (PEG-4000) and LMW chitosan were purchased from Sigma-Aldrich Co. (St. Louis, MO, USA). Chloroform HPLC grade: Honeywell Riedel-de Haen (Seelze, Germany). 0.9%

sodium chloride, methyl alcohol, and absolute ethyl alcohol: El-Nasr Pharmaceutical Chemicals Co. (Abuzaabal, Cairo, Egypt). Sorbitan monolaurate (Tween 20), Sorbitan monopalmitate (Span 40), Sorbitan monostearate (Span 60), Sorbitan laurate (Span 20) and cholesterol from lanolin: Merck Schuchardt OHG (Hohenbrunn, Germany). Chitosan and Polyethylene glycol 4000 (PEG-4000) were bought from Sigma-Aldrich Company (St. Louis, MO, USA). Sodium chloride (NaCl), potassium dihydrogen orthophosphate (KH2PO4), and sodium hydrogen phosphate (Na2HPO4): Oxford Laboratory (Mumbai, India). The National Research Center's Pharmaceutical Technology department (Cairo, Egypt) sent us potassium phosphotungstate as a gift. Aluminum chloride ($AlCl_3$): Glentham Life Sciences Ltd. (Planegg, Germany). Loba Chemie (Mumbai, India) provided the glass beads. Throughout the investigation, double-distilled water was utilized. The remaining reagents were all analytical quality.

2.2. Methods

2.2.1. Preparation of thymol-loaded niosomes (THYM-NIO)

Thymol-encapsulated and blank niosomal formulations were fabricated via a modified thin-film hydration technique [53–55]. A total of 100 mg of the lipid phase, comprising the selected non-ionic surfactant and cholesterol at the predetermined molar ratios, was accurately weighed. Thymol, (20 - 40 mg), depending on the formulation design, was subsequently incorporated into the same organic phase and co-dissolved with the lipid components in chloroform in a tapered round-bottom flask to obtain a clear and homogeneous solution. The solution was exposed to evaporation using a Büchi-M/HB-140 vacuum rotary evaporator (Flawil, St. Gallen, Switzerland) equipped at 50 rpm for 30 min. The flask was maintained in a thermostatically controlled water bath at $55 \pm 2\,^{\circ}C$ under lowered pressure, leading to the formation of a thin, dry film of the surfactant/cholesterol mixture along the inner surface after complete solvent removal. Subsequently, 20 mL of distilled water and ten 4 mm glass beads were added, and the flask was rotated under the same conditions for 20 min to achieve uniform hydration of the lipid film [53,56]. The hydrated dispersion was subjected to vortex mixing using a bench-top laboratory vortex mixer operating at approximately 2500 rpm for 10 min to ensure complete detachment of the lipid film and homogeneous vesicle dispersion. Vesicle size reduction was subsequently achieved using a bath-type sonicator operating at a fixed frequency of 40 kHz for 15 min. As bath sonicators operate in continuous mode and do not allow adjustment of amplitude or pulse parameters, reproducibility was ensured by strictly standardizing the sonication duration, frequency, sample volume, and central vial positioning across all batches. The bath temperature was continuously monitored using a digital thermometer and maintained at $45 \pm 2\,^{\circ}C$ to prevent overheating, vesicle destabilization, or potential drug degradation. These carefully controlled conditions ensured consistent vesicle size reduction and high batch-to-batch reproducibility. All formulations were prepared in triplicate to further confirm the reliability of the preparation process [57–59].

2.2.2. Preliminary screening study

Prior to implementation of the Box–Behnken experimental design, preliminary formulations were prepared to establish suitable formulation boundaries. The selection of formulation variables was guided by established niosomal researches [60–63], which identify surfactant hydrophilic - lipophilic balance (HLB), cholesterol molar ratio, and drug concentration as critical determinants of vesicle size, surface charge, and entrapment efficiency. Accordingly, investigative formulations (T1 - T12) were prepared by varying surfactant HLB values (4.7, 6.65, 8.6, and 16.7), cholesterol molar ratios (0.5 - 1.5), and thymol concentrations (20 - 40 mg). The selected HLB values corresponded to Span 60, Span 40, Span 20, and Tween 80, respectively. The composition codes and physicochemical characterization results of the preliminary formulations are presented in Table 1.

To evaluate the independent influence of each formulation variable, comparative statistical analyses were conducted by selecting formulation pairs in which two variables were kept constant while varying the third. The effect of HLB was examined across formulations T1, T4, T7, and T10, while cholesterol influence was evaluated through comparisons of T5 vs. T6 and T8 vs. T9. Drug loading impact was assessed using T2 vs. T3 and T11 vs. T12.

2.2.3. Experimental design for the optimization of THYM-NIO

THYM-loaded NIO were optimized using the Box-Behnken design (BBD) [54,64]. The experimental design was optimized to evaluate three independent variables: HLB of Span (X_1, value), cholesterol concentration (X_2, molar ratio), and THYM concentration ($\times_3$, mg), with the objective of minimizing mean particle size (Y_1) while maximizing zeta potential (Y_2) and entrapment efficiency (Y_3). The independent variables and their corresponding levels are summarized in Table 2, whereas the formulation compositions corresponding to the 15 experimental trials, including three center-point replicates, are summarized in Table 3. The associations between the measured responses and the selected independent factors were described using polynomial regression models, which were processed and evaluated with Statgraphics® Centurion XV software (version 15.2.05; StatPoint, Inc., Warrenton, VA, USA). Model adequacy and statistical relevance were determined through analysis of variance (ANOVA). Finally, BBD succeeded in predicting the optimized formulation (OF) by analyzing the influence of the input variables on the selected responses, accounting for all significant interactions as presented in Table 4.

Table 1
Codes, compositions and characterization of the preliminary study of THYM-NIO.

Formulae	Composition			Characterization		
	*HLB (value)	Cholesterol concentration (Molar ratio)	Drug amount (mg)	Particle size (nm ± SD)	Zeta potential (mV ± SD)	Entrapment efficiency (% ± SD)
T1	4.7	0.5	20	361.34 ± 4.11	−46.22 ± 1.37	86.71 ± 2.54
T2	4.7	1	30	426.77 ± 7.54	−36.97 ± 2.29	78.38 ± 1.87
T3	4.7	1	40	510.54 ± 6.78	−38.82 ± 3.79	89.66 ± 2.23
T4	6.65	0.5	20	250.39 ± 3.75	−36.89 ± 2.67	71.99 ± 1.67
T5	6.65	1	30	266.31 ± 2.66	−33.59 ± 1.11	63.11 ± 2.45
T6	6.65	1.5	30	386.99 ± 3.24	−27.94 ± 1.55	52.39 ± 2.99
T7	8.6	0.5	20	115.39 ± 2.67	−26.11 ± 1.97	35.96 ± 1.37
T8	8.6	1	30	198.25 ± 3.12	−25.13 ± 2.32	44.37 ± 2.33
T9	8.6	1.5	30	227.22 ± 3.66	−14.97 ± 1.56	32.69 ± 2.11
T10	16.7	0.5	20	103.78 ± 1.33	−20.38 ± 3.69	22.66 ± 3.87
T11	16.7	0.5	30	192.34 ± 2.39	−22.11 ± 3.33	26.22 ± 2.97
T12	16.7	0.5	40	213.97 ± 4.55	−22.63 ± 1.63	34.97 ± 1.99

*HLB value of 4.7 (Span 60), 6.65 (Span 40), 8.6 (Span 20) and 16.7 (Tween 80).

2.2.4. Formulation of PEGylated THYM-chitosomes

Optimized formula of THYM-NIO (OF) was further surface functionalized by application of PEG, chitosan or both to create PEGylated THYM-NIO (P-OF), THYM-Chitosomes (CH-OF) and PEGylated THYM-Chitosomes (PCH-OF), respectively. PEGylated THYM-NIO was prepared as previously described except by addition of 30 mg of PEG-4000 to the cholesterol/span blend. For the preparation of chitosomes and PEGylated chitosomes, a chitosan solution (0.5% w/v) was first prepared by dissolving 1 g of chitosan in 200 mL of aqueous 3% (v/v) acetic acid under continuous magnetic stirring at approximately 500 rpm at 25 °C for 24 h until a clear and homogeneous solution was obtained. The solution was subsequently filtered to remove any undissolved particulates. Thereafter, 5 mL of the chitosan solution was added to 5 mL of the previously prepared nanovesicle dispersion, and the mixture was subjected to magnetic stirring at 600 rpm for 24 h at room temperature to ensure uniform polymer adsorption and effective electrostatic interaction between chitosan and the vesicular surface without compromising vesicle structural integrity [65–67]. The codes and compositions of the surface-modified THYM-loaded THYM-NIO are detailed in Table 5.

2.2.5. Characterization of THYM-NIO

2.2.5.1. Evaluation of the PS, PDI and ZP of THYM-NIO. The mean particle size (PS) and polydispersity index (PDI) of the freshly prepared THYM-NIO were determined at 25 °C using dynamic light scattering (DLS) (Litesizer 500, Anton Paar, Austria). Prior to measurement, the samples were diluted tenfold with deionized water to minimize multi-scattering effects [68,69]. The same apparatus was used to confirm ZP based on electrophoretic mobility. The findings were the averages of three measurements.

2.2.5.2. Determination of EE%. Free (unentrapped) thymol was separated from vesicle-associated drug by centrifugation using a refrigerated high-speed bench-top centrifuge (Centurion Scientific Ltd., UK) equipped with a fixed-angle rotor at a gearing force of 15,000×*g* for 60 min at 4 °C. The supernatant containing free thymol was carefully collected, and the vesicle pellet was re-dispersed in cold buffer and re-centrifuged under identical conditions. This washing step was repeated three times to ensure complete removal of unentrapped drug and to minimize the risk of entrapment efficiency overestimation. The final washed pellet was lysed in methanol to disrupt the vesicles and release the entrapped thymol. The amount of thymol was quantified spectrophotometrically at 274 nm using a visible spectrophotometer (Jasco V-630, Tokyo, Japan) [55,70]. EE% was then calculated using the following formula:

$$\textit{Entrapment efficiency}\ (EE\%) = \frac{\textit{amount of drug entrapped}}{\textit{total amount of drug}} \times 100 \qquad \text{(Eq. 1)}$$

The UV–visible spectrophotometric method used for thymol quantification was validated with respect to linearity, specificity, and precision. Calibration curves were constructed over a concentration range of 10–70 μg/mL using the corresponding blank formulations as references. Detailed calibration data are provided in the Supplementary Data (Fig. S1).

2.2.5.3. Transmission electron microscopy (TEM). The ultrastructural features and bilayer organization of the vesicles, as well as their particle dimensions, were examined using transmission electron microscopy (TEM; JEM-2100, JEOL, Japan). A droplet of the niosomal suspension was deposited onto a carbon-coated copper grid and allowed to stand briefly to facilitate particle adsorption onto the support film. A piece of filter paper was used to eliminate any excess dispersion. After adding 1 drop of the staining solution (1% phosphotungstic acid solution), the excess solution was eliminated by using the tip of a filter paper to adsorb the liquid. Before being examined under an electron microscope, the material was allowed to air dry [66,71–73].

2.2.5.4. In-vitro release of THYM from NIO. The dialysis membrane approach, as defined in earlier research was employed to estimate the profile of THYM release for 24 h at 37 °C from fabricated niosomal formulae [60,74–76]. A volume of 3 mL of thymol nano formulation was transferred to a dialysis membrane bag (MWCO 13000) measuring 5 cm long and 2.1 cm broad. The study was conducted in different release media to simulate the GIT and blood microenvironments as follows: HCl buffer (pH 1.2) to mimic stomach and Phosphate buffers (pH 6.8 and 7.4) to mimic intestinal and blood pHs, respectively. The knotted dialysis bag was immersed in 50 mL of release media to maintain sink conditions throughout the experiment. Also, Free thymol was prepared as an aqueous suspension by dispersing 30 mg thymol in 20 mL PBS (pH 7.4), followed by vortex mixing at 2500 rpm for 5 min and bath sonication at 40 KHz for 10 min to obtain a uniform dispersion (1.5 mg/mL). An aliquot of equal volume (equivalent to 4.5 mg thymol) was immediately transferred into the dialysis bag and subjected to release testing under identical experimental conditions.

A rotary shaker (GLF 3203; Hilab, Düsseldorf, Germany) was used to conduct the release test. At 37 °C, the shaker's speed was adjusted to 150 strokes per minute. Sample aliquots (3 ml) were collected at intervals of 0.5, 1, 2, 4, 6, 8, 12, and 24 h and immediately replaced by equivalent quantity of fresh buffer. The conditions for the release of free thymol were the same as those for the control. The results were shown as a percentage of cumulative THYM release across three replicates after samples were spectrophotometrically analyzed at 274 nm according to established calibration curves Fig. S1.

To evaluate the release kinetics, the in vitro release profile of THYM from niosomes was fitted to various kinetic models including, zero-order, first-order, second-order, Hixson–Crowell, Baker–Lonsdale, and Higuchi diffusion. The model yielding the highest correlation coefficient (r) was considered the best fit for describing THYM release behavior [77].

Table 2
Independent formulation variables and dependent responses employed in the Box–Behnken design for the optimization of THYM-NIO.

Independent variables	Levels			Units
	Low (−1)	Medium (0)	High (1)	
X_1: [a]HLB of non-ionic surfactant	4.6	6.7	8.6	Value
X_2: Cholesterol concentration	0.5	1	1.5	Molar ratio
X_3: Drug Concentration	20	30	40	mg
Dependent variables	**Units**			**Goals**
Y_1: Particle Size	nm			Minimize
Y_2: Zeta Potential	mV			Maximize
Y_3: Entrapment efficiency	%			Maximize

[a] HLB: Hydrophilic lipophilic balance.

Table 3
Experimental run codes, compositions, and corresponding responses as generated by the Box–Behnken design.

Formulae	Factors			Responses		
	*X_1 (Value)	*X_2 (Molar ratio)	*X_3 (mg)	**Y_1 (nm± SD)	**Y_2 (mV± SD)	**Y_3 (% ± SD)
F1	6.65	0.5	40	259.01 ± 3.44	−37.00 ± 1.35	80.20 ± 1.03
F2	6.65	1	30	263.12 ± 2.75	−33.61 ± 2.64	61.32 ± 2.10
F3	8.6	1.5	30	230.99 ± 1.02	−17.00 ± 0.98	32.51 ± 0.93
F4	4.7	0.5	30	394.03 ± 2.01	−48.50 ± 2.47	94.74 ± 2.67
F5	6.65	1	30	261.00 ± 4.56	−33.82 ± 1.77	60.39 ± 4.68
F6	6.65	1.5	40	381.22 ± 3.08	−30.00 ± 1.11	54.58 ± 3.77
F7	8.6	1	40	210.45 ± 1.06	−25.03 ± 1.35	50.00 ± 3.99
F8	8.6	0.5	30	122.37 ± 1.47	−29.93 ± 2.03	42.64 ± 1.58
F9	6.65	0.5	20	253.04 ± 2.74	−35.41 ± 1.96	72.33 ± 3.69
F10	4.7	1	20	423.14 ± 4.78	−39.67 ± 2.48	79.53 ± 1.88
F11	6.65	1	30	261.80 ± 1.67	−31.06 ± 3.68	63.77 ± 1.65
F12	8.6	1	20	193.00 ± 3.78	−22.21 ± 1.06	34.83 ± 3.55
F13	4.7	1.5	30	518.00 ± 4.97	−38.90 ± 4.22	74.16 ± 2.12
F14	4.7	1	40	502.03 ± 5.95	−40.81 ± 3.41	85.50 ± 2.46
F15	6.65	1.5	20	337.81 ± 2.64	−29.93 ± 1.44	38.42 ± 1.33
***OF	****5.66	0.5	30.34	296.85 ± 1.59	−41.66 ± 2.85	81.00 ± 1.63

*X_1: HLB value, X_2: Cholesterol concentration and X_3: drug amount. Data is presented as mean ± standard deviation (SD).
**Y_1: particle size, Y_2: zeta potential and Y_3: entrapment efficiency of THYM.
*** OF: optimized formula.
****HLB was obtained by using a mixture of span 40 (31.7 mg) and span 60 (36.7 mg).

Table 4
Box–Behnken experimental design showing the estimated effects of the investigated factors and the corresponding *p*-values for the responses (Y_1–Y_3).

Factors	Y_1		Y_2		Y_3	
	Factor effect	*p*-value	Factor effect	*p*-value	Factor effect	*p*-value
X_1	−179.091	*0.0001	−3.262	*0.0001	−17.830	*0.0001
X_2	−40.339	*0.0000	−9.273	*0.0029	−45.061	*0.0017
X_3	−13.214	*0.0042	0.533	0.3755	−0.940	*0.0274
X_1^2	10.337	*0.0007	−0.072	0.8267	0.034	0.9627
X_1X_2	−3.846	0.5001	−0.846	0.5036	2.676	0.3603
X_1X_3	−0.794	*0.0300	0.012	0.8358	0.117	0.4156
X_2^2	60.033	*0.0383	4.200	0.4187	−3.850	0.7359
X_2X_3	1.860	0.1314	−0.075	0.7566	0.414	0.4609
X_3^2	0.307	*0.0023	−0.007	0.5443	0.005	0.8568

Y_1: particle size (nm), Y_2: zeta potential (mV) and Y_3: entrapment efficiency of THYM (%).
X_1: HLB value, X_2: Cholesterol Molar ratio, and X_3: drug amount (mg).
X_1X_2, X_1X_3, X_2X_3 are the interaction terms between the factors.
X_1^2, X_2^2, X_3^2 are the quadratic terms of the factors.
* Indicates a significant effect of factors on individual responses.

2.2.5.5. Fourier-transform infrared spectroscopy (FTIR). To verify the successful surface coating of niosomes (NIO) with polyethylene glycol (PEG) and chitosan (CH), Fourier Transform Infrared (FTIR) spectroscopy was carried out using a Thermo Scientific Nicolet iS10 (USA). Spectra of the lyophilized optimized formulation (OF), double-coated formulation (PCH-OF), and individual components (PEG and CH) were recorded over the range of 350–3500 cm^{-1} to identify characteristic functional groups and assess potential intermolecular interactions indicative of successful coating [78,79].

Briefly, 2 mL of each formulation were frozen at −70 °C for 6 h using a deep freezer (Daihan, WUF-25, Daihan Scientific Co., Ltd.), followed by lyophilization for 36 h under vacuum (Christ Alpha 1-4 LSC Plus, Martin Christ Gefriertrocknungsanlagen GmbH). Sucrose (1:1 w/w) was incorporated as a cryoprotectant to maintain vesicular integrity during the freeze-drying process [80].

2.2.6. Effect of storage

THYM-loaded niosomes were tested for stability in a refrigerator. The mixture was stored for three months at 4 °C in glass-sealed vials. Samples were taken at predefined intervals (0, 1, 2, and 3 months) and examined for changes in particle size, PDI, zeta potential, and entrapment efficiency in order to assess the impact of storage on THYM-loaded niosomes [81].

2.2.7. In-vivo evaluation of THYM-NIO

2.2.7.1. Study protocol and Induction of AD-Like Rat model. The animal experiments were performed in accordance with the protocol approved by the Research Ethics Committee of the Faculty of Pharmacy, Zagazig University (Approval no.: ZU-IACUC/3/F/28/2024). Eighty-four male Wistar rats (4–5 weeks old, 180–220 g) were acclimated for 12 h prior to the study under standardized conditions, including a temperature of 25 °C, relative humidity of 55 ± 10%, and a 12-h light/dark cycle [82]. The animals were randomly assigned into seven experimental groups, with each group consisting of twelve subjects, as outlined below:

Group 1: Negative control (NC), AD was not induced and no treatment was given.
Group 2: Positive control (PC), AD was induced and no treatment was given.
Group 3: AD was induced and rats were treated orally by Free THYM suspended in 0.5% CMC-Na.
Group 4: AD was induced and rats were treated orally by optimized THYM-NIO (OF).

Table 5
Identification codes, compositions, and physicochemical features of PEG/chitosan-coated optimized THYM-NIO.

**Formulae	*Composition of surface modification		Physicochemical features		
	PEG (mg)	Chitosan (CH) (1%, mL)	Particle size (nm ± SD)	Zeta potential (mV ± SD)	Entrapment efficiency (% ± SD)
OF	-	-	296.85 ± 1.59	−41.66 ± 2.85	81.00 ± 1.63
P-OF	30	-	384.46 ± 2.64	−33.50 ± 2.06	83.85 ± 2.98
CH-OF	-	5	444.37 ± 3.82	+33.16 ± 2.91	84.52 ± 3.67
PCH-OF	30	5	520.71 ± 4.94	+35.61 ± 2.43	88.91 ± 1.29

*All formulae were prepared using span 40 (31.7 mg), span 60 (36.7 mg), cholesterol (0.5 M ratio) and 30.33 mg drug. Values are expressed as the mean ± standard deviation (SD).
** OF: optimized formula, P-OF: PEGylated optimized formula, CH-OF: chitosomes and PCH-OF: PEGylated chitosomes.

Group 5: AD was induced and rats were treated orally by PEGylated THYM-NIO (P-OF).
Group 6: AD was induced and rats were treated orally by THYM-chitosomes (CH-OF).
Group 7: AD was induced and rats were treated orally by PEGylated THYM-chitosomes (PCH-OF).

AD was induced by administration of 70 mg/kg $AlCl_3$, i.p. weekly for up to 5 weeks before the experiment [8,83–85]. All treatments were administered at 30 mg/kg, P.O. of THYM daily for 5 weeks [8]. At the end of treatments, Neurobehavioral tests, including the Y-maze and the Morris water maze were conducted. Twenty-four hours following the conclusion of the behavioral testing, rats were killed via cervical dislocation under mild anesthesia, and their brains were immediately dissected, cleaned with ice-cold saline, and separated into two groups, each containing 6 rats. Hippocampal and cortical tissues from the first group were rapidly excised, homogenized in ice-cold 50 mM Tris-HCl buffer containing 300 mM sucrose (10% w/v, pH 7.4), and stored at −80 °C for biochemical analysis [86,87]. In the second batch, the brains were fixed in 10% (v/v) neutral buffer formalin for 24 h before histopathological examination [88].

2.2.7.2. Behavioral tests

2.2.7.2.1. Spatial working memory. It is a type of neurocognitive function linked to neural circuits in the hippocampus and prefrontal cortex. The Y-maze is a commonly employed tool for evaluating spatial working memory in different animal models [89,90]. Rats are placed in a Y-shaped maze with three identical arms set 120° apart. Recording begins once the rat is positioned in arm A, after which it is allowed to explore all arms freely for 4 min. From the recordings, the total number of arm entries (TAE) and alternations were recorded. An entry is defined as the rat fully crossing into an arm with all four paws. An alternation is recorded when the rat consecutively visits all three arms (A, B, and C) in any order. Spontaneous alternations percent (SAP%), an indicator of spatial working memory, is then calculated using the following formula [91].

$$SAP\% = \left[\frac{Number\ of\ alternations}{TAE - 2}\right] * 100 \quad \text{Eq. (2)}$$

2.2.7.2.2. Long-term spatial memory. Spatial learning and memory were assessed using the Morris water maze, employing a circular tank (180 cm diameter × 80 cm height) filled with room-temperature water to a 25 cm depth [92]. During the training phase, a platform was positioned at the center of the pool, elevated about 2.5 cm above the water surface so it remained visible to the rats. Training took place over five consecutive days, with each rat completing one 90-s trial per day. Initially, the rats swam around the pool's perimeter in search of an exit, but over time they learned to locate and climb onto the platform. On day five, immediately after the final training session, following removal of the platform, each rat was released into the pool from a starting point located in the quadrant opposite to the former platform position. During this probe test, the time spent exploring the target quadrant was subsequently quantified [93,94].

2.2.7.3. Biochemical analysis

2.2.7.3.1. Oxidative biomarkers. MDA, GSH, SOD and GPx.

The Lipid Peroxidation assay Kits, (Cat. #K739-100, K464-100 and K335-100, Bio Vision Inc., Milpitas, USA), were used to determine the concentration of MDA, GSH and SOD respectively, in the supernatant of brain tissue homogenate. Colorimetric spectrophotometric method was employed and The results were reported as nmol/mg protein for MDA and GSH and U/mg for SOD levels [95–98].

Finally, enzyme-linked immunosorbent assay (ELISA) was applied to estimate the level of GPx using a Kit (Cat. #E1172Ra, Biolinkk, Delhi, India). The amount of GPx was expressed as ng/mg protein.

2.2.7.3.2. Proinflammatory cytokines

TNF-α and IL-1β

Proinflammatory cytokines, TNF-α and IL-1β, were measured using ELISA kits, (Cat. #E0117Mo and E0119Ra, Bioassay Technology Lab, Shanghai, China, respectively) [99,100]. The data obtained was expressed as ng/mg tissue protein.

2.2.7.3.3. Neurochemical markers

GFAP, DA and Aβ

The Sandwich-ELISA concept was adopted to estimate the level of Glial fibrillary acidic protein (GFAP) in the hippocampus tissue homogenates using ELISA kit (Cat. # E-EL-R1428, Elabscience Bionovation Inc., Houston, Texas, USA). The concentration of the protein is expressed as ng/mg tissue protein [99,100]. Also, Dopamine level (DA) was estimated by using the same technique using ELISA kit (Cat. # CSB-E08660r, CUSABIO TECHNOLOGY, Houston, Texas, USA) and displayed as ng/mg tissue. Moreover, the beta-amyloid (Aβ) levels were estimated using rat-enzyme-linked immunoassay (ELISA). The used kit (Cat. # orb410690, Biorbyt LLC, San Francisco, USA) and the concentration was demonstrated as Pg/mg tissue protein [101].

2.2.7.4. Histopathological examination. Following a 24-h fixation in 10% neutral buffered formalin, the collected cerebral cortex specimens were progressively dehydrated through a series of increasing ethanol concentrations, cleared with xylene, and then encased in paraffin wax. Sections of 5 μm thickness were prepared, stained with hematoxylin and eosin (H&E), and inspected under a microscope for histopathological alterations [102,103]. All tissue sections were imaged using a swift microscope equipped with a swift digital camera.

2.2.8. Statistical analysis

Statistical analyses were conducted with GraphPad Prism 8 (GraphPad Inc., La Jolla, CA, USA), using data from in vitro experiments (n = 3) and in vivo studies (n = 12 or n = 6), with results expressed as mean ± SD. Comparisons were performed using one-way or two-way ANOVA, followed by Tukey–Kramer post hoc test for multiple comparisons. Differences were considered statistically significant at $p < 0.05$.

3. Results and discussion

3.1. Preliminary screening

The preliminary screening results (Table 1) demonstrated that surfactant HLB, cholesterol molar ratio, and drug concentration significantly influenced vesicle characteristics. A clear HLB-dependent trend was observed across formulations T1, T4, T7, and T10, where increasing HLB resulted in a progressive reduction in entrapment efficiency and zeta potential magnitude ($p < 0.05$), accompanied by a significant decrease in vesicle size ($p < 0.05$). In particular, Tween 80-based formulations (HLB 16.7; T10 - T12) exhibited significantly lower entrapment efficiency and markedly reduced surface charge magnitude compared with formulations prepared using lower-HLB Span surfactants ($p < 0.05$). Although Tween-containing vesicles produced smaller particle sizes, their reduced drug retention capacity and lower zeta potential indicated compromised vesicular stability. This behavior is consistent with previously reported observations that high-HLB surfactants such as Tween 80 tend to form more fluid and less tightly packed bilayers compared with lower-HLB Span surfactants, thereby reducing encapsulation efficiency and vesicle stability [55,60,62]. Since thymol is a lipophilic compound, efficient encapsulation requires a compact hydrophobic bilayer domain; therefore, the looser bilayer organization associated with Tween 80 likely facilitated drug leakage and diminished entrapment efficiency.

Cholesterol molar ratio also exerted a statistically significant effect, as shown by comparisons between T5 vs. T6 and T8 vs. T9 ($p < 0.05$). Increasing cholesterol content resulted in vesicle enlargement and reduced entrapment efficiency and zeta potential magnitude, consistent with the role of cholesterol in modulating bilayer rigidity and membrane organization in niosomal systems [55,63]. Similarly, increasing drug concentration significantly increased vesicle size and influenced entrapment efficiency (T2 vs. T3; T11 vs. T12, $p < 0.05$), whereas no statistically significant effect was observed on zeta potential.

Collectively, these statistically and literature-supported findings justified the exclusion of Tween 80 (HLB 16.7) and enabled the selection of experimentally feasible and physically stable formulation ranges for subsequent optimization using the Box–Behnken design.

3.2. Response surface methodology for the optimization of THYM-NIO

The optimal formula (OF) of THYM-NIO was predicted using a BBD with multiple regression analysis utilizing two-ways ANOVA after the values of the factors were established. Table 4 summarizes factor effects and p-values for particle size (PS, Y_1), zeta potential (ZP, Y_2), and THYM entrapment efficiency (EE%, Y_3), with $p < 0.05$ considered significant. These effects were further validated by Pareto charts (Fig. 1) and 3D response surface plots (Fig. 2).

3.2.1. Effect on particle size (Y_1)

According to Table 3, the mean PS of all niosomal formulas ranged from 122.37 ± 1.47 (F8) to 518.00 ± 4.97 nm (F13), exhibiting PDI values < 0.24, reflecting monodispersity of the nanosystem. The following equation, which was obtained from the data analysis, indicates that the quadratic model was the best match for the PS as determined by multiple regression analysis:

$$\textit{Mean vesicle Size } (Y_1) = 1224.0 - 179.091\ X_1 - 40.3397\ X_2 - 13.2141\ X_3 + 10.3375\ X_1^2 - 3.84615 \times 1 \times 2 - 0.794872 \times 1 \times 3 + 60.0333\ X_2^2 + 1.86 \times 2 \times 3 + 0.307583\ X_3^2 \quad \text{(Eq.3)}$$

Analysis of Table 4, Figs. 1A and 2A indicates that X_1 (HLB value), X_2 (cholesterol molar ratio), and X_3 (drug amount) were the primary factors influencing the mean particle size of THYM-loaded niosomes. Among these, cholesterol content (X_2) exhibited a pronounced synergistic effect on particle size (Y_1). This effect is exemplified by the differences observed between formulations (F1 and F6), (F8 and F3), and (F4 and F13), where, at constant levels of X_1 and X_3, elevating the cholesterol ratio from 0.5 to 1.5 resulted in corresponding increases in mean particle size from 259.01 ± 3.44 to 381.22 ± 3.08 nm, 122.37 ± 1.47 to 230.99 ± 1.02 nm, and 394.03 ± 2.01 to 518.00 ± 4.97 nm, respectively. These findings are consistent with previously reported studies highlighting the impact of cholesterol content on the particle size of niosomes [61,104,105].

The influence of cholesterol on vesicle size cannot be attributed solely to increased membrane rigidity. Cholesterol intercalates between surfactant alkyl chains, modulating bilayer packing density, phase behavior, and membrane curvature elasticity. At low to moderate cholesterol concentrations, this intercalation enhances bilayer order and mechanical stability while decreasing membrane permeability, often resulting in the formation of relatively smaller and more uniform vesicles due to reduced defects and tighter packing. In contrast, at higher cholesterol molar ratios, excessive packing density disrupts the optimal curvature elasticity of the bilayer. This reduction in membrane flexibility increases curvature stress, which can favor the formation of larger vesicles as the system minimizes bending energy under constrained packing conditions. Additionally, high cholesterol content may promote vesicle fusion or aggregation, further contributing to increased particle size [106,107].

Conversely, it was discovered that HLB (X1) had a substantial negative influence on mean particle size (Y1). A notable illustration of the influence of HLB on particle size was the difference in particle size observed where, at equal levels of X_2 (cholesterol ratio) and X_3 (drug quantity), increasing the value of HLB from 4.7 to 8.6 resulted in a drop in mean particle size from 518.00 ± 4.97 to 230.99 ± 1.02 nm, 394.03 ± 2.01 to 122.37 ± 1.47 nm and 502.03 ± 5.95 to 210.45 ± 1.06 nm for (F13 and F3), (F4 and F8) and (F14 and F7), respectively. These results are consistent with prior reports demonstrating the influence of HLB value on the particle size of nanovesicles [54,108,109]. This behavior can be explained by surfactant molecular geometry, where higher-HLB surfactants possess greater headgroup hydration, promoting higher membrane curvature and formation of smaller vesicles. Conversely, lower-HLB surfactants favor thicker bilayers with lower curvature, resulting in larger vesicles [110].

Finally, Increasing drug concentration also resulted in a statistically significant enlargement of vesicle size as shown in (F9 and F1), (F12 and F7), (F10 and F14) and (F15 and F6) where, at the same values of HLB and cholesterol ratio, the particle size increased from 253.04 ± 2.74 to 259.01 ± 3.44 nm, 193.00 ± 3.78 to 210.45 ± 1.06 nm, 423.14 ± 4.78 to 502.03 ± 5.95 nm and 337.81 ± 2.64 to 381.22 ± 3.08 nm, respectively, by increasing drug amount from 20 to 40 mg. These findings could be attributed to increase in the viscosity of dispersion medium by raising the drug concentration, which in turn increases the shear stress effect and bilayer expansion due to incorporation of drug in the hydrophobic domain [111,112]. A similar outcome was observed for solid lipid nanoparticles loaded with ketoprofen [113].

3.2.2. Effect on zeta potential (Y_2)

ZP reflects niosomal stability, with higher values promoting particle repulsion and minimizing aggregation by overcoming van der Waals forces [114]. All niosomal formulations displayed a negative surface charge (Table 3), with zeta potential (ZP, Y_2) values varying between -17.00 ± 0.98 mV (F3) and -48.50 ± 2.47 mV (F4). Multiple regression analysis identified the best-fit significant model for ZP, as represented by the following equation:

$$\textit{Zeta Potential } (Y_2) = 59.0563 - 3.26249\ X_1 - 9.27308\ X_2 + 0.533494\ X_3 - 0.0723208\ X_1^2 - 0.846154 \times 1 \times 2 + 0.0128205 \times 1 \times 3 + 4.2\ X_2^2 - 0.075 \times 2 \times 3 - 0.00775\ X_3^2 \quad \text{(Eq. 4)}$$

Table 4, as well as Figs. 1B and 2B, reveal that HLB value (X_1) demonstrated a pronounced inhibitory effect on zeta potential (ZP)

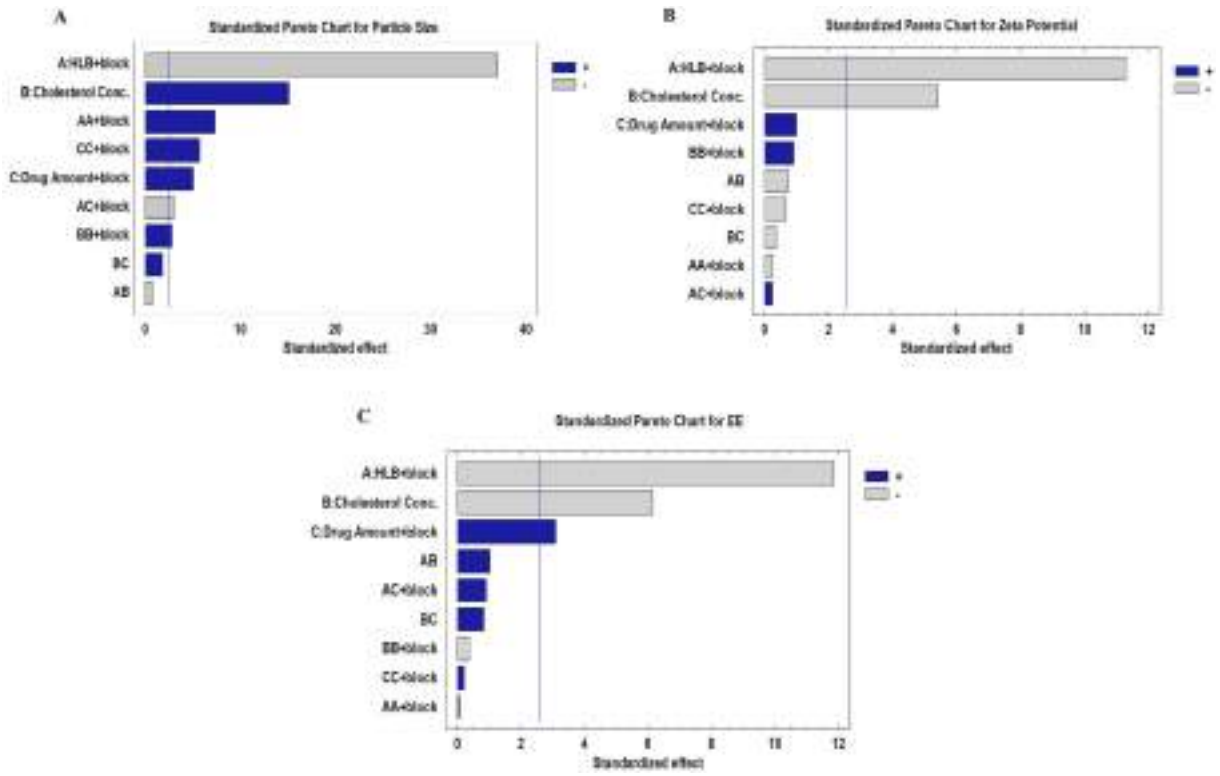

Fig. 1. Standardized Pareto diagrams show the impact of the studied variables on (A) particle size, (B) zeta potential, and (C) drug entrapment efficiency.

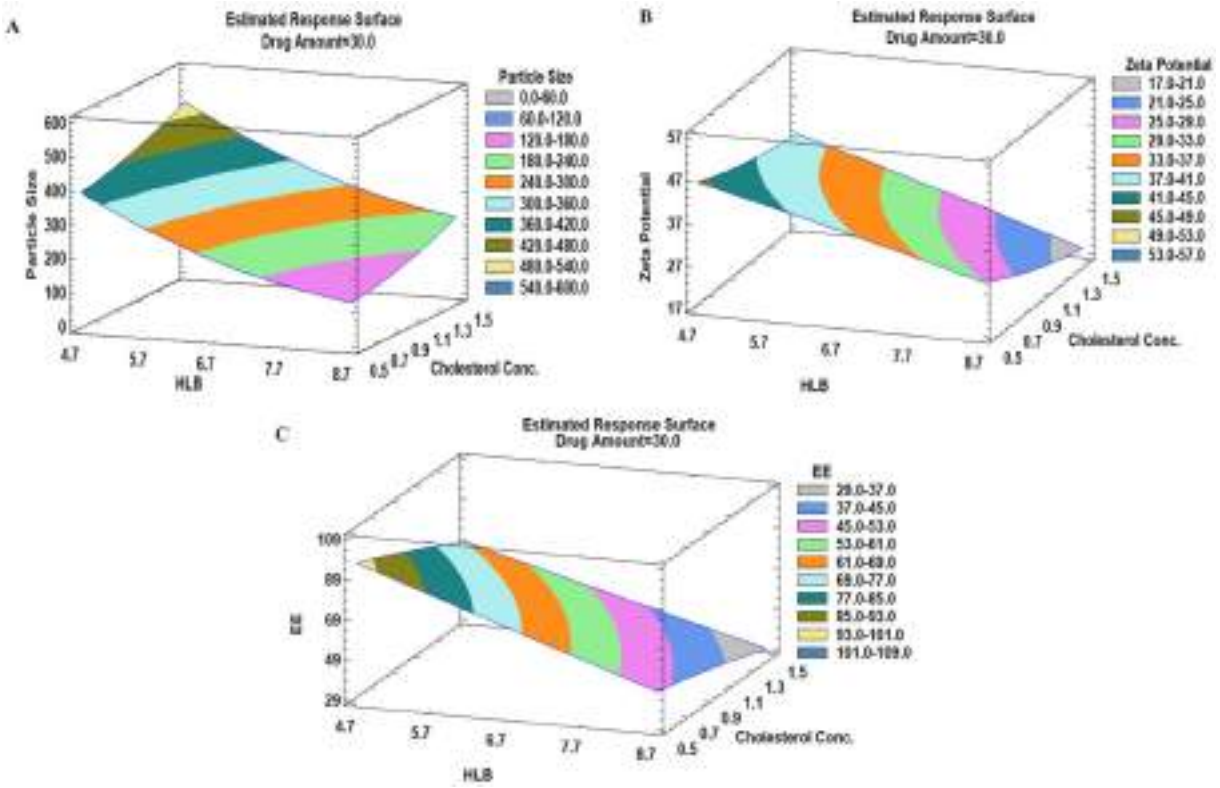

Fig. 2. 3D response surface and contour plots showing the influence of the formulation factors studied on (A) particle size, (B) zeta potential, and (C) entrapment efficiency.

values. For the niosomal formulation pairs F3 and F13, F8 and F4, and F7 and F14, a decrease in HLB value from 8.6 to 4.7, at constant levels of X_2 and X_3, led to an increase in ZP from -17.00 ± 0.98 to -38.90 ± 4.22 mV, -29.93 ± 2.03 to -48.50 ± 2.47 mV, and -25.03 ± 1.35 to -40.81 ± 3.41 mV, respectively. This behavior can be explained by the reduced hydrophilicity and tighter hydrophobic packing of low-HLB surfactants such as Span 60. Their lower degree of headgroup hydration promotes a more compact bilayer structure, which enhances preferential adsorption of hydroxyl ions at the vesicle interface and increases the magnitude of negative surface charge. In contrast, higher-HLB surfactants possess more hydrated and flexible headgroups, which can partially shield interfacial charge and reduce electrostatic potential. Therefore, variations in bilayer packing density and interfacial hydration directly influence surface charge distribution and electrostatic stabilization in non-ionic vesicular systems [115].

A similar trend was observed for cholesterol concentration (X_2), where lowering the cholesterol ratio from 1.5 to 0.5 at constant X_1 and X_3 increased ZP from -30.00 ± 1.11 to -37.00 ± 1.35 mV (F6 vs. F1). Conversely, increasing cholesterol from 0.5 to 1.5 at constant HLB and drug levels decreased ZP from -29.93 ± 2.03 to -17.00 ± 0.98 mV (F8 vs. F3). Increasing cholesterol content reduced the magnitude of zeta potential by altering the interfacial electrical environment of the vesicles. In non-ionic surfactant systems, surface charge primarily arises from preferential adsorption of hydroxyl ions and orientation of polar headgroups at the vesicle–aqueous interface. Cholesterol modifies the polarity and dielectric properties of the interfacial region, leading to reduced availability of ionizable groups and diminished hydroxyl ion adsorption. This decreases the surface charge density and compresses the electrical double layer, resulting in a lower absolute zeta potential [55,56,106].

3.2.3. *Effect on entrapment efficiency (Y_3)*

Entrapment efficiency (EE%, Y_3) of all niosomal formulations ranged from $32.51 \pm 0.93\%$ (F3) to $94.74 \pm 2.67\%$ (F4). Multiple regression analysis identified the best-fit model for EE%, as represented by the following equation:

$$\textit{Entrapment Efficiency } (Y_3) = 197.614 - 17.8301\ X_1 - 45.0615\ X_2 - 0.940609\ X_3 + 0.0348455 \times_1^2 + 2.67692 \times 1 \times_2 + 0.117949 \times 1 \times_3 - 3.85 \times_2^2 + 0.414 \times 2 \times_3 + 0.005125 \times_3^2 \quad \text{(Eq.5)}$$

Examination of Table 4 and Fig. 1C and 2C demonstrates that all investigated variables significantly influenced entrapment efficiency ($p < 0.05$).

HLB value (X_1) was the primary factor influencing the entrapment efficiency (EE%) of THYM-loaded niosomes. Increasing the HLB value, while maintaining constant cholesterol concentration (X_2) and drug amount (X_3), led to a decrease in EE%. Specifically, as HLB increased from 4.7 to 6.65, the percentage of THYM entrapped decreased from $74.16 \pm 2.12\%$ to $32.51 \pm 0.93\%$ in F13 and F3, respectively. Similar looks were observed in F4 and F8, where raising the HLB from 4.7 to 8.6 reduced EE% from $94.74 \pm 2.67\%$ to $42.64 \pm 1.58\%$, and in F14 versus F7, where EE% declined from $85.50 \pm 2.46\%$ to $50.00 \pm 3.99\%$ with the same increase in HLB. This effect can be attributed to the longer alkyl chain of Span 60 (lower HLB), Lower-HLB surfactants enhance entrapment of lipophilic drugs as thymol by providing a more hydrophobic and densely packed bilayer environment. Increased hydrophobic domain integrity improves drug partitioning into the membrane core, thereby increasing encapsulation efficiency. Higher-HLB surfactants, due to increased bilayer fluidity and hydration, may reduce hydrophobic drug retention [60,116].

The observed reduction in entrapment efficiency at higher cholesterol concentrations can be attributed to competitive incorporation within the hydrophobic bilayer domain. At elevated concentrations (e.g., 1 M), this condensed bilayer structure reduces the available free volume for lipophilic drug accommodation. Since thymol preferentially partitions into the hydrophobic core, excessive cholesterol limits drug incorporation by occupying bilayer space and restricting molecular mobility. Consequently, increasing cholesterol beyond the optimal ratio leads to decreased drug entrapment efficiency. Additionally, cholesterol-induced ordering of alkyl chains decreases membrane fluidity and alters drug–bilayer partition equilibrium, while excessive cholesterol may reduce bilayer defects that facilitate drug entrapment. These competing structural and thermodynamic effects collectively account for the observed decline in encapsulation efficiency [106,107,116–119]. These findings were validated in (F8 and F3), (F14 and F13) and (F9 and F15) where by raising the cholesterol ratio from 0.5 to 1.5 at the same HLB level and drug amount, EE% decreased from 42.64 ± 1.58 to $32.51 \pm 0.93\%$, 85.50 ± 2.46 to $74.16 \pm 2.12\%$ and 72.33 ± 3.69 to 38.42 ± 1.33, respectively.

Finally, it was clear that increasing drug loads in niosomal formulae significantly affected the EE%. Increasing drug load in niosomal formulae, at constant cholesterol and HLB level, from 20 to 40 mg increases EE% from 34.83 ± 3.55 to $50.00 \pm 3.99\%$, 79.53 ± 1.88 to $85.50 \pm 2.46\%$ for F10 and F14, respectively. These findings are consistent with previous reports, which demonstrated that higher drug loading results in increased nanoparticle size, thereby elongating the diffusion pathway into the aqueous phase, minimizing drug leakage, and consequently improving encapsulation efficiency [116,120]. Also, increasing drug concentration enhances encapsulation efficiency until saturation of the bilayer partitioning capacity is reached. Drug incorporation is governed by partition equilibrium between aqueous and lipid phases; higher drug availability increases bilayer loading until thermodynamic equilibrium is achieved [106].

The reduction in particle size and entrapment efficiency observed with increasing HLB values in the present study may be attributed to the influence of surfactant hydrophilicity on bilayer organization and vesicle curvature. However, the relationship between surfactant HLB and vesicular characteristics is not universal and is strongly influenced by other formulation parameters such as surfactant chemical structure, cholesterol content, drug lipophilicity, and preparation method. In one experimental comparison, niosomes prepared with the higher-HLB surfactant Tween 60 exhibited significantly larger particle sizes than those prepared with lower-HLB surfactants (Span 60 and Brij 72) under comparable cholesterol conditions, demonstrating that increasing HLB may be associated with enlarged vesicles in some systems [121]. Multivariate modeling has also shown that entrapment efficiency depends on several interacting formulation factors rather than HLB alone, indicating the need to interpret HLB effects within a broader compositional context [122]. Importantly, thymol is a highly lipophilic molecule that preferentially partitions into hydrophobic bilayer domains, making its encapsulation particularly sensitive to changes in bilayer hydrophobicity and structural organization. Accordingly, the trends observed in the present study should be interpreted within the compositional and drug-specific framework of the developed niosomal system rather than as a generalized rule.

Beyond statistical optimization, the optimized physicochemical characteristics were evaluated in the context of potential brain delivery. The optimized particle size (~296 nm) falls within the nanoscale range reported for vesicular systems investigated for blood–brain barrier (BBB) interaction Where smaller nanoparticles may favor passive diffusion through BBB.

The observed zeta potential values contribute to colloidal stability during systemic circulation, reducing aggregation and premature clearance. Stable nanosystems with controlled surface charge are less prone to rapid opsonization, thereby increasing the likelihood of vascular interaction with the BBB endothelium [123].

Additionally, the high entrapment efficiency ensures sufficient drug payload within each vesicle, which is critical for achieving therapeutically relevant concentrations at the target site following systemic administration. Efficient drug retention minimizes premature leakage in circulation and supports sustained release behavior upon reaching the

brain microenvironment.

Collectively, these physicochemical characteristics are consistent with nanosystems reported for brain delivery, where particle size, surface charge, and interfacial properties collectively influence interaction with the BBB rather than particle size alone, thereby supporting the translational relevance of the optimized formulation.

3.2.4. Model adequacy and optimization validation

The adequacy and predictive reliability of the developed quadratic models were evaluated according to established response surface methodology (RSM) validation principles, including assessment of model fit, predictive error, multicollinearity, and residual independence [124–126]. High coefficients of determination were obtained for particle size, zeta potential, and entrapment efficiency ($R^2 = 99.71\%$, 96.96%, and 97.44%, respectively), with corresponding adjusted R^2 values exceeding 91%, indicating strong explanatory power without evidence of overfitting. Low standard errors of estimation and mean absolute error values confirmed minimal predictive deviation between experimental and fitted responses. Variance inflation factor (VIF) values close to unity demonstrated absence of multicollinearity and confirmed the orthogonality of the Box–Behnken design, while Durbin–Watson statistics (1.96–3.25) indicated independence of residuals.

Simultaneous optimization of the responses was performed using a composite desirability function approach widely applied in pharmaceutical and analytical optimization studies [125,126]. The obtained overall desirability value (0.72) reflects a statistically acceptable and balanced compromise among the competing objectives of minimizing particle size while maximizing zeta potential and entrapment efficiency. The strong agreement between predicted and experimentally observed responses at the optimized formulation further confirms the robustness and reliability of the optimization strategy. The developed model demonstrated strong statistical significance and predictive capability, supported by high correlation coefficients and acceptable model adequacy indicators, confirming the robustness of the optimization process.

3.3. Selection and surface functionalization of THYM-NIO formula (OF)

According to the outcomes of the Box–Behnken design (BBD), which successfully fulfilled the optimization objectives of minimizing particle size while maximizing zeta potential and entrapment efficiency (EE%), an optimized formulation was developed in accordance with the predicted model. This formulation was subsequently evaluated to verify the predictive reliability of BBD model. The optimized formulation was prepared using the optimal levels of the independent variables, namely 5.6631, 0.5, and 30.33 for X_1, X_2, and X_3, respectively. Preparation was carried out using the thin-film hydration technique, followed by physicochemical characterization as previously described. The model-predicted responses for Y_1, Y_2, and Y_3 were 299.13 nm, −42.369 mV, and 84.57%, respectively, whereas the experimentally obtained values were 296.85 ± 1.59 nm, -41.66 ± 2.85 mV, and $81.00 \pm 1.63\%$, respectively, demonstrating close agreement between predicted and observed results. Subsequently, the optimized formulation was surface modified using polyethylene glycol (PEG), chitosan, or a combination of both. The compositions and corresponding codes of the optimized and surface-modified formulations are summarized in Table 5.

3.4. Characterization of fabricated optimized and surface modified THYM-NIO

3.4.1. Particle size and zeta potential

Nanovesicles' stability and efficiency were significantly affected by their particle size (P.S) and zeta potential (ZP) [127]. Therefore, these factors were evaluated and identified as key formulation parameters for all elaborated THYM-NIO. Data for P.S. and Z.P. of optimized formula and surface modified formulae are presented in Table 5. The statistical analysis using two-way ANOVA of these results revealed that modified niosomes containing either PEG or chitosan or both led to significant ($p < 0.0001$) increase in P.S. compared to uncoated nanovesicles. Also, PEGylated chitosomes showed the highest significant increase in particle size among all prepared THYM-NIO ($p < 0.0001$). These may be attributed to the increased coated layers by added polymers and it was in accordance with previous studies [81,128].

While PEG/chitosan coating increased the hydrodynamic diameter of PCH-OF to approximately 520 nm, transport across the blood–brain barrier (BBB) is not limited to passive transcellular diffusion, which primarily applies to small lipophilic molecules. Nanocarriers can access the brain through active cellular processes such as adsorptive-mediated transcytosis (AMT) and receptor-mediated transcytosis (RMT), which are strongly influenced by surface charge and surface chemistry rather than size alone [129,130]. The positive surface charge imparted by chitosan can enhance electrostatic interaction with the negatively charged luminal membrane of brain endothelial cells, promoting AMT-dependent uptake. Additionally, PEGylation prolongs systemic circulation and increases the likelihood of endothelial interaction [131]. Importantly, the superior in vivo pharmacodynamic performance of PCH-OF in the present study provides functional confirmation of effective brain delivery despite the increased hydrodynamic diameter. Therefore, the translational relevance of the coated formulation is supported by established BBB transport mechanisms and experimental biological outcomes.

In terms of ZP, all formulations showed high stability (i.e., below −30 mV or above +30 mV) [77]. PEGylation of THYM-loaded nanovesicles resulted in a decrease in zeta potential. This observation aligns with previously reported findings, which demonstrate that the ethylene oxide chains of PEG reduce the surface charge by shifting the shear plane toward the aqueous phase, resulting in decreased zeta potential values regardless of the intrinsic charge of the nanocarriers [81,132,133] Coating nanovesicles with chitosan (a cationic polymer) changed the ZP values from negative to positive, as seen by the ZP of CH-OF and PCH-OF formulae [134]. However, it is important to acknowledge that positively charged nanocarriers may exhibit increased plasma protein adsorption and potential rapid clearance. The incorporation of PEG is expected to mitigate these effects by providing steric stabilization and reducing opsonization [135].

3.4.2. Entrapment efficiency (EE%)

EE% of prepared coated and uncoated THYM-NIO are presented in Table 5. It was clear that there was an increase but non-significant ($p>0.05$) difference between amount of drug entrapped in the optimized formula and the single coated formulae (P-OF and CH-OF). On the other hand, double coated THYM-NIO (PCH-OF) had a significant ($p = 0.0141$) increase in EE% if compared to uncoated OF. The enhanced encapsulation efficiency observed with the double-coated nanovesicles can be attributed to a synergistic interaction between chitosan and PEG. Chitosan, being a positively charged polymer, strengthens electrostatic interactions with THYM, favoring its retention within the vesicular core. PEG, on the other hand, provides a steric barrier that stabilizes the vesicle surface and reduces drug leakage by preventing diffusion into the external medium. When applied individually, chitosan improves EE primarily via electrostatic attraction, while PEG mainly limits drug leakage. However, when combined as a double coating, the cationic nature of chitosan and the steric hindrance from PEG act together: chitosan actively attracts and binds THYM molecules, and PEG simultaneously stabilizes the vesicular surface, reducing drug loss. This combined coating resulted in higher encapsulation efficiency compared to either coating alone, suggesting an additive effect of PEG and chitosan on drug retention within the vesicular system [66,67].

Also, a popular and successful technique for enhancing the properties of many drug delivery systems is the modification of nanocarriers by the addition of PEG. The reduction of undesired interaction with biological components and the prevention of complex aggregation are two benefits of PEGylation of nanocarriers. Moreover, PEG can serve as a hydrophilic

ligand linker, improving the targeting efficiency of the drug delivery system. Additionally, PEGylation helps maintain the physicochemical stability of chitosomes, preventing undesirable alterations [136].

To conclude, the incorporation of PEG into chitosomes enhanced their surface stability by providing a steric barrier that reduces particle aggregation and minimizes drug leakage. Consequently, this structural stabilization contributed to superior drug retention, as evidenced by the significantly higher entrapment efficiency observed in PEGylated chitosomes compared to non-PEGylated counterparts [81]. This improvement underscores the dual role of PEG in both stabilizing the vesicular architecture and optimizing drug encapsulation.

3.4.3. *Transmission electron microscopy (TEM)*

The TEM micrographs (Fig. 3) verified the successful formation of well-defined, spherical nanovesicles with a bilayer structure. Particles of PEGylated vesicles had a more spherical form than those of non-PEGylated vesicles which was consistent with beforehand reported data [137]. Regarding chitosomes or PEGylated chitosomes, The irregular layer observed around the particles may result from a drug-rich core encased within a chitosan surface coating [66]. The particle dimensions depicted in the micrographs corroborate a high concordance with those determined via DLS analysis.

3.4.4. *In vitro release profile of THYM-NIO*

Fig. 4 demonstrates the in vitro release patterns of THYM from the niosomal formulations in comparison with free THYM at different pHs (1.2, 6.8 and 7.4). Free thymol exhibited rapid and nearly complete release (~100%) within 6 h at all tested pHs, confirming unrestricted diffusion in the absence of a carrier matrix. Its release was significantly higher than all vesicular formulations at corresponding time points ($p < 0.05$). Given that thymol is a chemically stable phenolic compound that does not undergo significant hydrolytic degradation within the physiological gastrointestinal pH range [28,138], the differences observed in release behavior are attributed to formulation-dependent diffusion control rather than intrinsic pH-induced instability.

At 24 h, all niosomal systems exhibited sustained release relative to the free drug ($p < 0.05$). Across all tested pH conditions, cumulative release consistently followed the order OF > P-OF > CH-OF > PCH-OF. At pH 7.4, cumulative release values were $84.90 \pm 2.30\%$, $76.90 \pm 2.80\%$, $68.20 \pm 1.89\%$, and $63.80 \pm 1.23\%$ for OF, P-OF, CH-OF, and PCH-OF, respectively. Comparable results were obtained at pH 6.8, where release reached $85.78 \pm 3.88\%$, $76.78 \pm 1.97\%$, $68.20 \pm 1.89\%$, and $63.80 \pm 1.23\%$, respectively. Under acidic conditions (pH 1.2), cumulative release was $86.11 \pm 3.68\%$, $75.97 \pm 1.38\%$, $74.12 \pm 2.22\%$, and $66.78 \pm 2.78\%$ for OF, P-OF, CH-OF, and PCH-OF, respectively.

Statistical analysis demonstrated that the uncoated formulation (OF) exhibited significantly higher release than all coated systems across pHs 1.2, 6.8, and 7.4 ($p < 0.05$). At pH 6.8 and 7.4, P-OF released significantly more drug than CH-OF ($p < 0.05$), whereas under acidic conditions (pH 1.2), no statistically significant difference was observed between P-OF and CH-OF ($p > 0.05$). Importantly, the dual-coated formulation (PCH-OF) showed significantly lower cumulative release compared with OF, P-OF, and CH-OF at all tested pH conditions ($p < 0.05$).

Mechanistically, the pH-independent behavior of PEGylated vesicles arises from the neutral, non-ionizable structure of polyethylene glycol, which preserves steric stabilization and membrane integrity throughout the physiological pH range [115,135]. Conversely, chitosan contains primary amine groups ($pK_a \approx 6.3$–6.5) that become protonated under acidic conditions, leading to reversible polymer hydration and swelling rather than structural degradation [139]. The dual PEG–chitosan

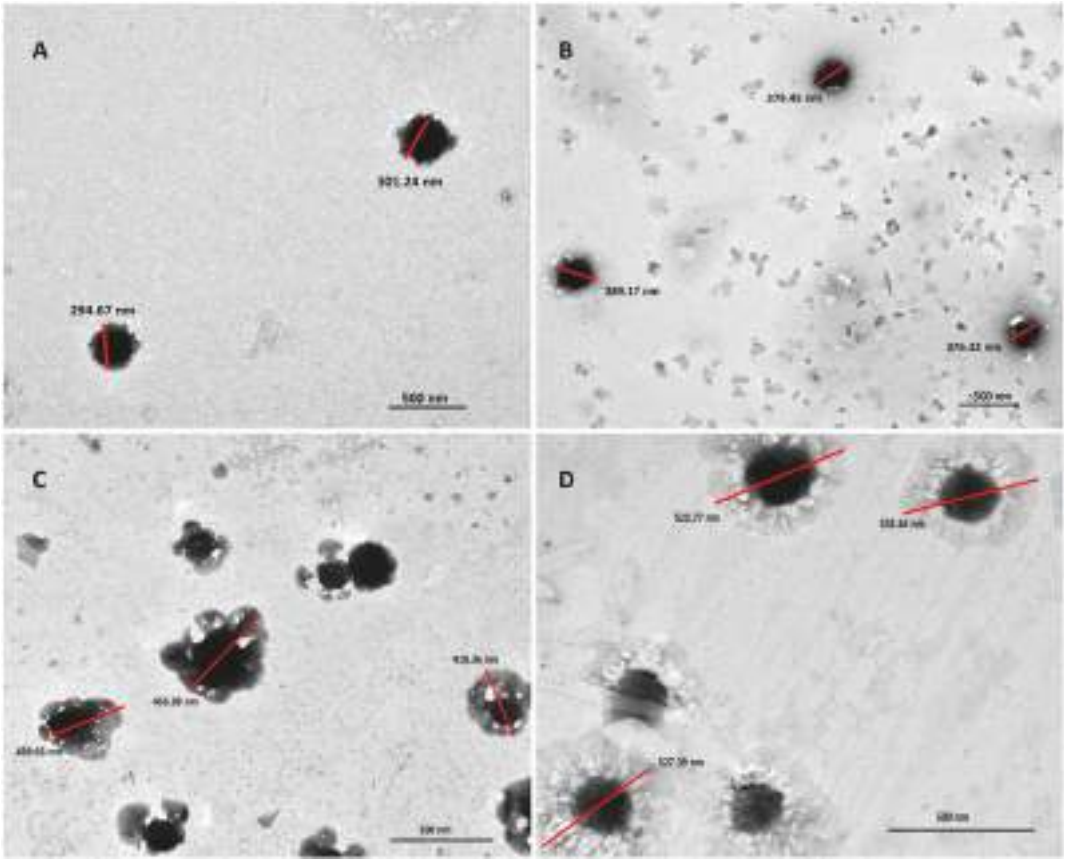

Fig. 3. Transmission electron microscopy (TEM) images depicting the dimensional characteristics and morphological features of optimized THYM-NIO (OF) (A), PEGylated THYM-NIO (P-OF) (B), Chitosomes (CH-OF) (C) and PEGylated chitosomes (PCH-OF) (D).

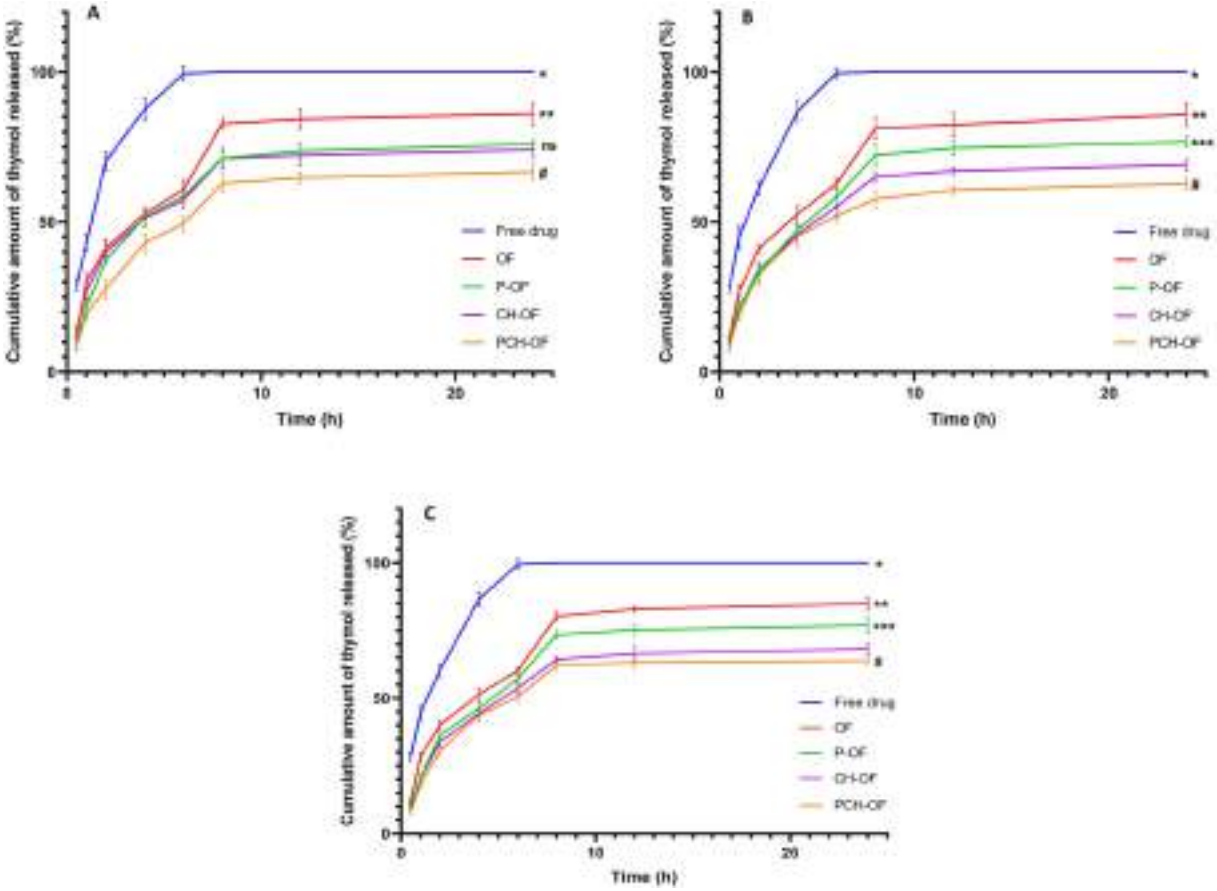

Fig. 4. Cumulative in vitro release of THYM from free drug solution, optimized niosomes (OF), PEGylated niosomes (P-OF), chitosan-coated niosomes (CH-OF), and PEGylated chitosan-coated niosomes (PCH-OF) over 24 h at pH 1.2 (A), pH 6.8 (B) and pH 7.4 (C). Results are expressed as mean ± SD (n = 3).
Note: * denotes a significant difference for all tested formulae (THYM-NIO) compared to Free THYM ($p < 0.05$), ** denotes a significant difference for all coated formulae (P-OF, CH-OF and PCH-OF) compared to uncoated optimized formula (OF) ($p < 0.05$), ***denotes a significant difference between PEGylated niosomes (P-OF) and chitosomes (CH-OF) ($p < 0.05$), #denotes a significant difference between chitosomes PEGylated chitosomes (PCH-OF) compared to chitosomes (CH-OF) and PEGylated niosomes (P-OF) ($p < 0.05$).

functionalization in PCH-OF likely moderates excessive swelling, thereby maintaining controlled diffusion even in gastric conditions. The absence of burst release further confirms preservation of vesicular structural integrity. Overall, thymol release from the developed nanovesicles was governed predominantly by vesicular bilayer diffusion and surface modification rather than medium pH, with PCH-OF providing the most sustained and statistically distinct release profile across all investigated conditions.

Notably, the drug release from the niosomal formulations exhibited a biphasic profile, with an early fast release of surface-adsorbed THYM, afterwards a prolonged, controlled release phase lasting up to 24 h [77,140]. Optimized uncoated formula showed significant higher release pattern ($p < 0.0001$) over all coated THYM-NIO. Among the formulations, the PCH-OF system, featuring a dual PEG/chitosan coating, exhibited the slowest release profile compared to the singly coated P-OF and CH-OF formulations. This pronounced retardation is likely attributable to the combined barrier and sustained-release effects conferred by the PEG and chitosan layers on the nanocarriers [66,128]. To further elucidate the drug release mechanisms, quantitative kinetic modeling was performed for all formulations at pH 1.2, 6.8, and 7.4 by fitting the release data to zero-order, first-order, second-order, Hixson–Crowell, Baker–Lonsdale, and Higuchi diffusion models. As presented in Table S1 (Supplementary Data), the Higuchi model consistently provided the best fit, yielding the highest correlation coefficients (r) across all formulations and pH conditions, indicating that THYM release from niosomal systems is predominantly diffusion controlled.

Based on the Higuchi model (Table S1), OF exhibited correlation coefficients of 0.943, 0.937, and 0.954 at pH 1.2, 6.8, and 7.4, respectively. In comparison, P-OF showed r values of 0.932, 0.934, and 0.922; CH-OF demonstrated 0.947, 0.951, and 0.938; while PCH-OF exhibited the highest correlation coefficients of 0.964, 0.958, and 0.956 under the corresponding pH conditions, indicating stronger conformity to diffusion-controlled release behavior [77].

Sustained and controlled drug release is particularly relevant in Alzheimer's disease (AD), which is characterized by chronic neuroinflammation, oxidative stress, and progressive neuronal dysfunction requiring continuous therapeutic modulation rather than transient exposure. Persistent activation of inflammatory and degenerative pathways contributes to disease progression, and maintaining relatively stable CNS drug concentrations may enhance therapeutic consistency and reduce pharmacodynamic fluctuations [141,142]. Nanocarrier-based delivery systems have been proposed as strategies to improve brain drug retention and prolong therapeutic activity by reducing burst release and supporting sustained drug availability within the neural microenvironment [130]. Given the reported antioxidant and anti-inflammatory properties of thymol, the observed extended-release profile may therefore align with the chronic pharmacodynamic requirements of neurodegenerative therapy.

3.4.5. Fourier-transform infrared spectroscopy (FTIR)

The successful coating of the optimized formula with PEG and CH was verified by Fourier Transform Infrared spectroscopy (FTIR) via

comparative spectral analysis of the uncoated formulation, pure polymers, and the double-coated system (PCH-OF) as shown in Fig. 5.

The FTIR spectrum of the optimized niosomal formulation (Fig. 5A) exhibited characteristic peaks at 3329.88 cm^{-1}, corresponding to O–H stretching vibrations of hydroxyl groups present in both sorbitan moieties (Span surfactants) and cholesterol. The peaks at 2918.69–2853.04 cm^{-1} are attributed to asymmetric and symmetric C–H stretching of long alkyl chains, confirming the presence of Span (40/60) and cholesterol. The absorption band at 1732.58 cm^{-1} corresponds to ester carbonyl (C=O) stretching of Span, while the peak at 1675.64 cm^{-1} can be assigned to C=C stretching of cholesterol. Peaks observed at 1459.27–1376.24 cm^{-1} represent CH_2 bending vibrations of the long alkyl chains of Span surfactants and cholesterol, while the band at 1049.09 cm^{-1} is attributed to C–O stretching vibrations of the ester linkage in Span (sorbitan moiety). These features collectively confirm the successful formation of the lipid-based niosomal structure [78,79].

The FTIR spectrum of PEG (Fig. 5B) showed a broad band at 3450.29 cm^{-1} corresponding to O–H stretching of terminal hydroxyl groups. The peak at 2879.18 cm^{-1} is assigned to C–H stretching of methylene groups. The bands at 1462.46 cm^{-1} and 1344.22 cm^{-1} correspond to CH_2 bending, twisting, and wagging vibrations. A strong and characteristic peak at 1102.85 cm^{-1} is attributed to C–O–C ether stretching, representing the repeating oxyethylene units of PEG and serving as its fingerprint peak [143].

The FTIR spectrum of chitosan (Fig. 5C) exhibited a broad peak at 3365.92 cm^{-1}, corresponding to overlapping O–H and N–H stretching vibrations. The peaks at 2974.88–2876.07 cm^{-1} are due to aliphatic C–H stretching. The bands at 1647.48 cm^{-1} (Amide I) and 1590.12 cm^{-1} (Amide II/N–H bending) indicate the partially acetylated nature of chitosan. The peaks at 1375.41–1310.53 cm^{-1} are attributed to C–N stretching and CH_2 bending, while those at 1065.12–1022.69 cm^{-1} correspond to C–O–C and C–O stretching vibrations of the polysaccharide backbone, which are typical for the pyranose ring of Chitosan [79,143].

For the double-coated formulation (PCH-OF, Fig. 5D), the FTIR spectrum exhibited notable changes compared to the individual components. A broadened band at approximately 3300 cm^{-1} corresponds to overlapping O–H stretching vibrations (from Span, cholesterol, and PEG) and N–H stretching vibrations (from chitosan), indicating intermolecular hydrogen bonding.The C–H stretching bands showed a slight

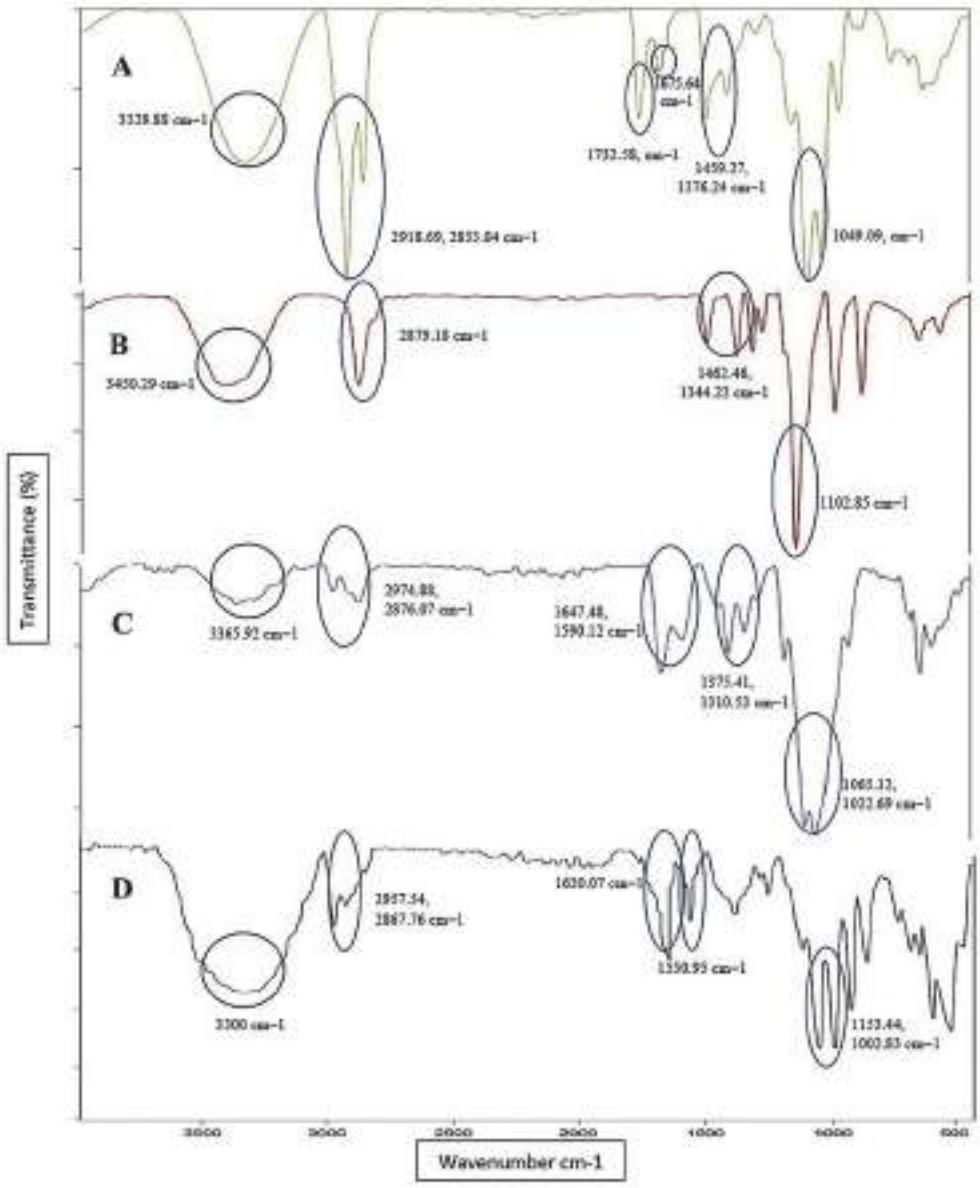

Fig. 5. FTIR spectra of: (A) Optimized formula (OF), (B) Pure PEG, (C) Pure Chitosan and (D) PEGylated Chitosomes (PCH-OF).

shift to 2957.54–2867.76 cm^{-1}, suggesting alterations in the alkyl chain environment. Notably, the Amide I band shifted from approximately 1647 cm^{-1} to 1630.07 cm^{-1}, accompanied by the appearance of a distinct Amide II band at 1550.95 cm^{-1}, confirming the presence of chitosan on the niosomal surface. Furthermore, the characteristic PEG ether band appeared broadened and slightly shifted within the range of 1153.44–1002.83 cm^{-1}, overlapping with the glycosidic (C–O–C) vibrations of chitosan, indicating successful incorporation of both polymers. The disappearance of the ester carbonyl peak (~1732 cm^{-1}) further supports the interaction between the niosomal components and the coating polymers. Overall, the observed peak shifts, band broadening, and intensity changes provide strong evidence of intermolecular interactions, confirming the successful dual coating of niosomes with PEG and chitosan [78,79].

3.5. Effect of storage

3.5.1. Effect of storage on the Homogeneity of the THYM- NIO

During the three-month stability investigation at the storage temperature (4 °C), all prepared THYM-NIO (OF, P-OF, CH-OF and PCH-OF) Exhibited excellent physical stability, with no sedimentation, absence of coarse particles, no phase separation, and no observable change in color.

3.5.2. Storage-induced variations in particle size, surface charge, and drug entrapment of THYM-NIO

It was necessary to inspect the effect of coating by PEG/Chitosan on the stability of THYM-NIO on their stability upon storage for 3 months at 4 °C, with the aim of minimizing drug leakage from niosomal formulae. PS, ZP and EE% values were assessed at the end of each month of the storage period, as presented in Fig. 6. Stability assessments were conducted on Days 30, 60, and 90 and compared with baseline (Day 0) measurements. Across all nanovesicular formulations, an increase in mean particle size accompanied by a gradual decline in both zeta potential (ZP) and entrapment efficiency (EE%) was observed over the storage period. The initial vesicle sizes for OF, P-OF, CH-OF and PCH-OF were 296.85 ± 1.59, 384.46 ± 2.64, 444.37 ± 3.82 and 520.71 ± 4.94 nm, respectively. After 90 days of storage at 4 °C, these values increased to 335.90 ± 1.51, 391.22 ± 2.5, 450.92 ± 2.93 and 526.62 ± 7.14 nm, respectively.

Statistical analysis demonstrated a significant increase ($p < 0.0001$) in the vesicle size of the uncoated OF formulation after 90 days of storage, Fig. 6A. This size enlargement was primarily attributed to the coagulation of nano-colloidal dispersion. In contrast, P-OF, CH-OF and PCH-OF exhibited a non-significant ($p > 0.05$) size increase on Day 90. Overall, the growth rate of PEGylated and chitosan-coated NIO was markedly lower than that of uncoated NIO, which can be attributed to the additional PEG and/or chitosan layers imparting enhanced steric stabilization. This steric barrier effectively reduced vesicle–vesicle interactions and coagulation, thereby limiting particle growth [144,145]. It should be noted that PDI of all niosomal formulae remained below 0.3 over the whole storage period indicating homogenous dispersions.

Zeta potential values exhibited slight reductions over the storage duration, changing from −41.66 ± 2.85, −33.50 ± 2.06, +33.16 ± 2.91 and 35.61 ± 2.43 mV for OF, P-OF, CH-OF and PCH-OF, respectively, to −32.80 ± 4.45, −30.86 ± 1.02, +31.96 ± 3.63 and +32.90 ± 1.88 mV after 90 days. Despite this decline, the changes were statistically significant only in case of uncoated OF ($p = 0.0018$) and non-significant in case of all coated formulae ($p > 0.05$), and the ZP values remained sufficiently high to ensure adequate electrostatic repulsion, thereby maintaining colloidal stability, Fig. 6B.

Regarding entrapment efficiency, Fig. 6C illustrates a significant reduction ($p < 0.0005$), ($p = 0.0085$) and ($p = 0.0451$) in EE% for the OF, P-OF and PCH-OF formulations, decreasing from 81 ± 1.63, 83.58 ± 2.98, 84.52 ± 3.67% on Day 0 to 73.56 ± 1.96, 78.10 ± 1.52 and 79.91 ± 1.42% on Day 90, respectively. Conversely, the EE% of double coated formula, PCH-OF, decreased non-significantly

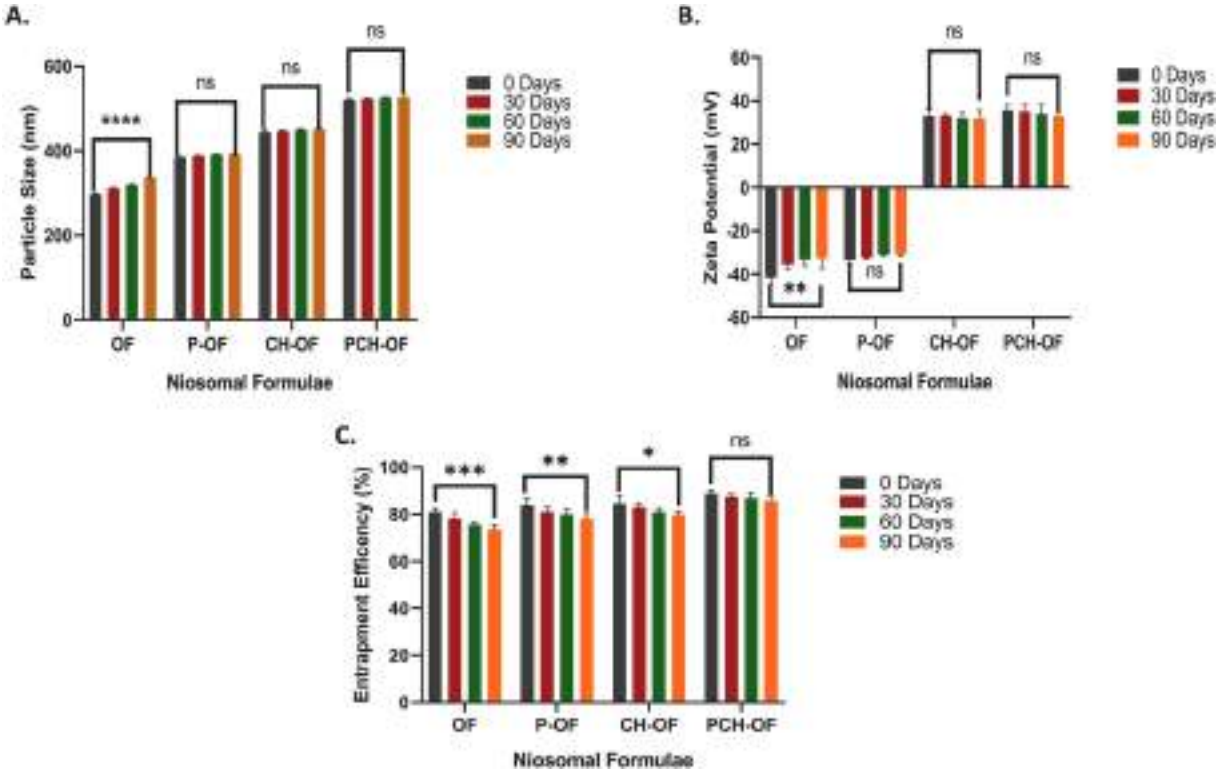

Fig. 6. Impact of Storage on: **A.** Particle size, **B.** Zeta potential and **C.** Entrapment efficiency of THYM-NIO (OF), PEGylated THYM-NIO (P-OF), THYM-Chitosomes (CH-OF), PEGylated THYM-Chitosomes (PCH-OF). Data is presented as mean ± SD, (n = 3). ***Note:*** levels of significance: * denotes $p < 0.05$, ** $p < 0.01$, *** $p < 0.001$ and **** $p < 0.0001$ while ns refers to a non-significant change.

($P = 0.2954$) over the same period, from $88.91 \pm 1.29\%$ to $85.91 \pm 1.99\%$. This minimal drug leakage observed in the modified formulations is likely due to the presence of surface double coatings, which act as diffusion barriers and limit drug expulsion from the lipid matrix [145].

Overall, the stability study demonstrated that all NIO formulations remained within acceptable physicochemical limits throughout the storage period. However, PEGylated and chitosan-coated NIO exhibited superior stability profiles, underscoring the critical role of surface modification in enhancing the long-term stability of span-based nanovesicular systems.

3.6. In vivo pharmacodynamic assessment of THYM-NIO

3.6.1. Behavioral assessment

3.6.1.1. Y-maze test. The neuroprotective effects of free THYM and THYM-loaded niosomes (THYM-NIO) against $AlCl_3$-induced learning and memory deficits were evaluated using behavioral assays. In the Y-Maze test, the positive control group exhibited a marked reduction in spontaneous alternation performance (SAP%). Treatment with free THYM and all THYM-NIO formulations significantly improved cognitive performance ($p < 0.05$) compared to the positive control (Fig. 7A). Notably, all THYM-NIO formulations demonstrated superior enhancement of spatial working memory, as evidenced by a further significant reduction in SAP% relative to free THYM ($p < 0.05$). Among the formulations, the PCH-OF system, featuring dual PEG/chitosan coating, elicited the most pronounced decrease in SAP%, indicating its superior efficacy in enhancing memory performance compared to all other treatment groups (Fig. 7A). These results underscore the potentiated cognitive benefits conferred by the double-coated THYM-NIO formulation.

3.6.1.2. Morris water maze (MWM). The Morris Water Maze (MWM) test demonstrated that treatment with free THYM and THYM-loaded niosomal formulations effectively mitigated the learning and spatial memory deficits induced by $AlCl_3$ administration. This was evidenced by a significant increase in the time spent in the target quadrant compared to the $AlCl_3$-treated positive control group ($p < 0.05$; Fig. 7B), indicating improved memory retention and spatial navigation. Notably, the PCH-OF formulation, which features dual PEG/chitosan coating, produced the most pronounced effect, achieving the greatest reduction in escape latency and the longest duration spent in the target quadrant relative to all other treatment groups. These observations suggest that the dual-coated niosomal system more efficiently delivers THYM to the brain, thereby enhancing its neuroprotective and cognitive-restorative effects. Overall, the findings indicate that both free THYM and THYM-NIO formulations substantially restored the deficits in spatial learning and memory caused by $AlCl_3$, with PCH-OF showing superior efficacy, highlighting its potential as an effective strategy to improve cognitive function.

3.6.2. Alzheimer's biomarkers

3.6.2.1. Mitigated brain oxidative stress. As illustrated in Fig. 8A–D, $AlCl_3$ administration caused a marked increase in oxidative stress within the brain ($p < 0.0001$). This was evidenced by a significant elevation in malondialdehyde (MDA) levels, indicating enhanced lipid peroxidation, alongside substantial reductions in Major intrinsic antioxidant systems in neuronal cells, such as glutathione (GSH), superoxide dismutase (SOD), and glutathione peroxidase (GPx). These alterations reflect a disruption in the oxidative–antioxidant balance, leading to enhanced vulnerability of neurons to oxidative damage [146]. Collectively, the findings confirm that $AlCl_3$ induces severe oxidative stress, which likely contributes to the observed neurotoxicity and cognitive deficits [147–151]. Relative to the diseased positive control group, treatment with free THYM and THYM-NIO significantly decreased MDA levels while restoring antioxidant defenses, as evidenced by increased GSH, SOD, and GPx levels.

3.6.2.2. Attenuated brain inflammation. Rats with $AlCl_3$-induced Alzheimer's disease exhibited a pronounced upregulation of the pro-inflammatory cytokines TNF-α and IL-1β ($p < 0.0001$) compared to the negative control group, reflecting enhanced neuroinflammatory responses characteristic of AD pathology. Notably, treatment with free THYM and THYM-loaded nanocarriers markedly attenuated the levels of both TNF-α and IL-1β (Fig. 8E and F), demonstrating a potent anti-inflammatory effect and significant neuroprotective potential. Among the formulations, the dual-coated PCH-OF system produced the most pronounced reduction in pro-inflammatory cytokines, highlighting the enhanced efficacy of PEG/chitosan-coated THYM niosomes in mitigating $AlCl_3$-induced neuroinflammation and supporting cognitive

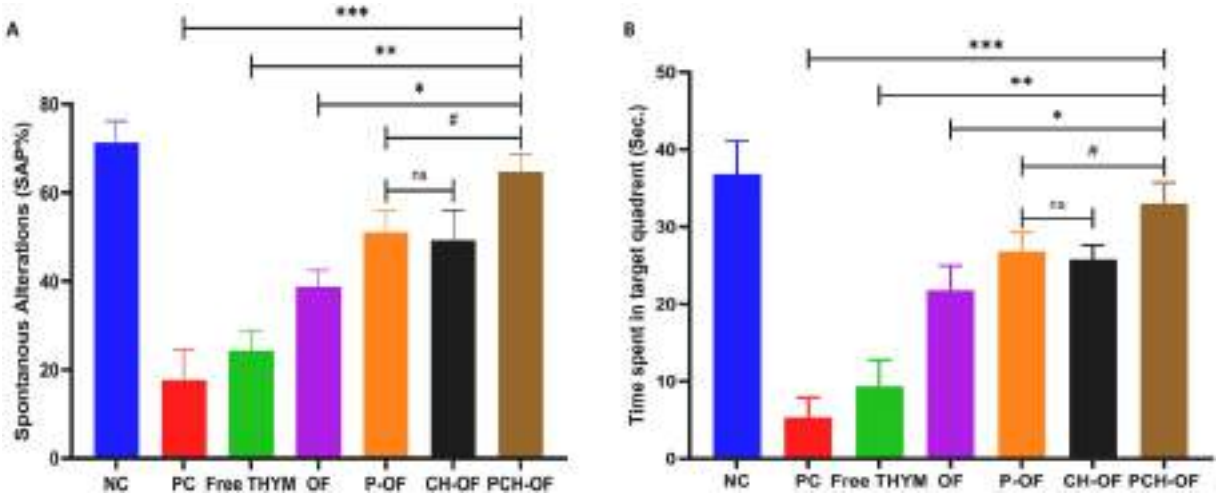

Fig. 7. A. Y-Maze test and **B.** Morris water maze test (MWM) of positive control (PC) and groups treated with: Optimized THYM-NIO (OF), PEGylated THYM-NIO (P-OF), THYM-Chitosomes (CH-OF) and THYM-PEGylated Chitosomes (PCH-OF). All measurements are reported as mean ± SD (n = 12). ***Note:*** *** denotes a significant difference from positive control group (PC), **denotes a significant difference from group treated with free THYM, * denotes a significant difference from group treated with optimized formula (OF), # denotes significant difference from group treated with PEGylated chitosomes (PCH-OF) while, ns indicates a non-significant effect. Significant effect when ($p < 0.05$).

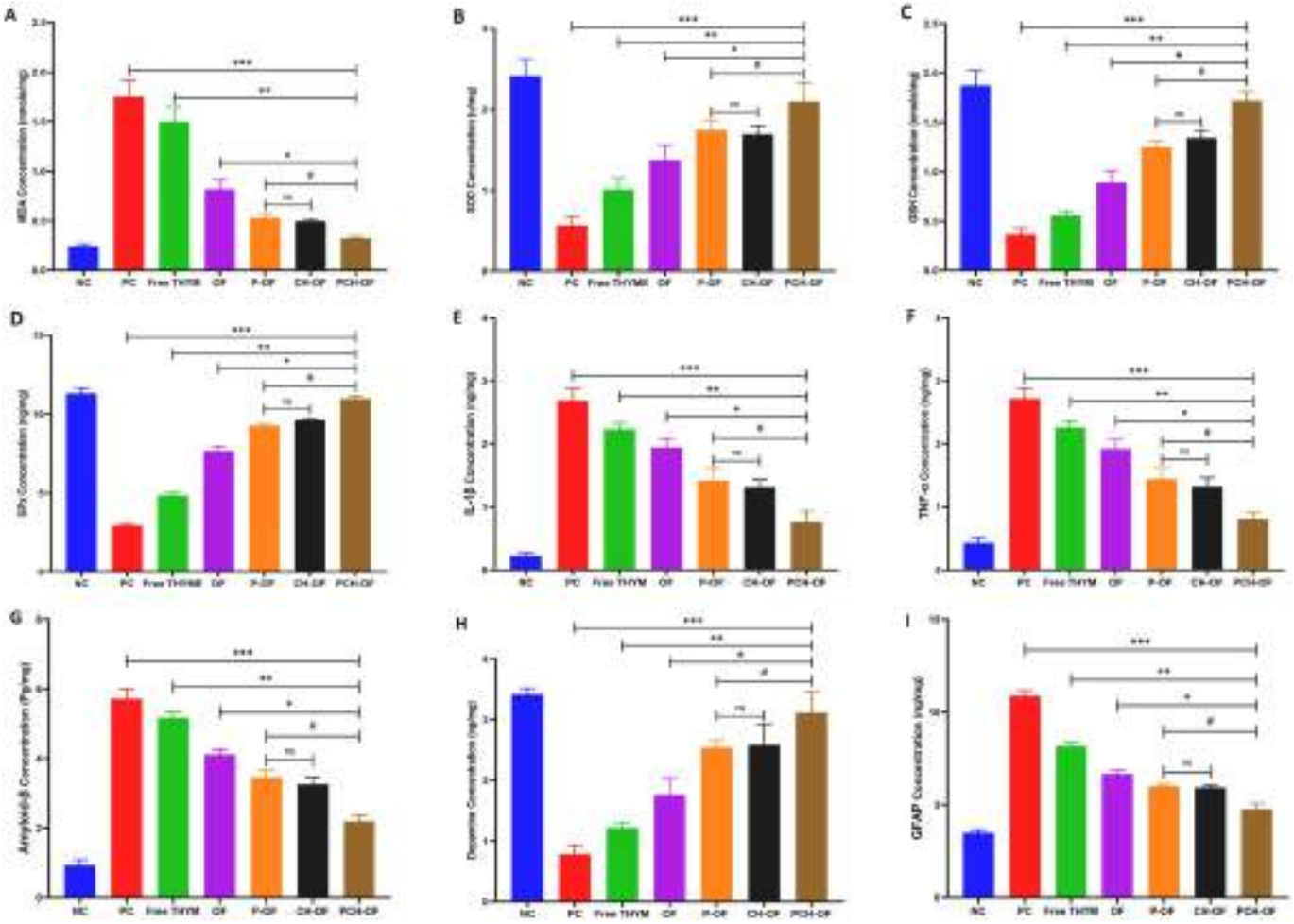

Fig. 8. Levels of Alzheimer's Biomarkers: **A.** Malondialdehyde (MDA), **B.** Superoxide dismutase (SOD), **C.** Glutathione (GSH), **D.** Glutathione peroxidase (GPx), **E.** Interleukin-1 beta (IL-1β), **F.** Tumor necrosis factor (TNF-α), **G.** Amyloid-beta (Aβ), **H.** Dopamine (DA) and **I.** Glial fibrillary acidic protein (GFAP) in experimental groups: NC (negative control), PC (positive control), OF (group treated with optimized THYM-NIO), P-OF (group treated with PEGylated THYM-NIO), THYM-chitosomes (group treated with CH-OF) and THYM-PEGylated chitosomes (group treated with PCH-OF). Data are presented as mean ± standard deviation (SD), (n = 6). ***Note:*** *** denotes a significant difference from positive control group (PC), **denotes a significant difference from group treated with free THYM, * denotes a significant difference from group treated with optimized formula (OF), # denotes significant difference from group treated with PEGylated chitosomes (PCH-OF) while, ns indicates a non-significant effect. Significant effect when ($p < 0.05$).

restoration [95,97,98,100,150].

3.6.2.3. Neurochemical markers. Glial fibrillary acidic protein (GFAP) serves as a key marker of astrocyte activation, with its elevated expression associated with the early stages of AD, contributing to reactive gliosis and subsequent neuronal injury. Beta-amyloid protein (Aβ), the primary constituent of senile plaques in AD brains, is significantly increased during disease progression. Additionally, a hallmark feature of AD is the reduction in brain dopamine (DA) levels, which correlates with cognitive and behavioral deficits. In line with these pathological changes, $AlCl_3$ administration in the diseased positive control group resulted in a significant increase in GFAP and Aβ levels, accompanied by a marked decrease in brain DA concentration ($p < 0.0001$) compared to the normal control group [99,148,152,153].

As illustrated in Fig. 8G–I, treatment with free THYM and THYM-NIO significantly reduced GFAP expression, reflecting their capacity to attenuate $AlCl_3$-induced astrocytic activation and neuroinflammation. These treatments also decreased brain Aβ levels and restored dopamine (DA) concentration, indicating amelioration of AD-related neurodegenerative changes. Collectively, these findings highlight the multifaceted neuroprotective potential of THYM and THYM-loaded niosomes, encompassing the mitigation of oxidative stress, enhancement of antioxidant defenses, suppression of neuroinflammation, and improvement of neuronal function in the context of AD.

The data presented for all biomarkers (Table 6 and Fig. 8) demonstrate that treatment with THYM-loaded niosomes produced significantly greater effects compared to free THYM ($p < 0.0001$; OF, P-OF, CH-OF, PCH-OF). Furthermore, uncoated niosomes (OF) were significantly less effective than the surface-modified formulations (P-OF, CH-OF, and PCH-OF; $p < 0.0001$), with the dual-coated PCH-OF exhibiting the most pronounced efficacy. These results confirm that PEGylation and chitosan functionalization enhance THYM availability into brain tissues, improving targeted delivery and therapeutic potential for AD. Our findings are consistent with previous studies demonstrating that surface modification strategies, such as PEGylation or chitosan coating, can effectively overcome the BBB and optimize central nervous system drug delivery [154–157].

3.6.3. Histopathological examination

Histological assessment of the cerebral cortex revealed distinct morphological variations among the experimental groups (Fig. 9A–G). The negative control group (Fig. 9A) exhibited normal cortical architecture, characterized by well-organized neuronal cell bodies of variable shapes, intact axons and dendrites, and normally distributed supporting

Table 6
Levels of biochemical markers in different experimental groups.

*Treatment Groups	**Biochemical Markers								
	MDA (nmole/mg)	SOD (u/mg)	GSH (nmole/mg)	GPx (ng/mg)	TNF-α (ng/mg)	IL-Iβ (ng/mg)	Aβ (ng/mg)	DA (ng/mg)	GFAP (ng/mg)
NC	0.25 ± 0.03	2.41 ± 0.22	1.87 ± 0.15	11.32 ± 0.36	0.46 ± 0.09	0.22 ± 0.06	0.92 ± 0.17	3.42 ± 0.10	3.49 ± 0.18
PC	1.75 ± 0.16	0.56 ± 0.10	0.36 ± 0.07	2.94 ± 0.13	2.72 ± 0.16	2.68 ± 0.19	5.72 ± 0.28	0.78 ± 0.16	10.87 ± 0.29
Free THYM	1.50 ± 0.15	1.01 ± 0.14	0.56 ± 0.05	4.87 ± 0.18	2.26 ± 0.11	2.23 ± 0.14	5.17 ± 0.16	1.22 ± 0.07	8.14 ± 0.21
OF	0.82 ± 0.09	1.38 ± 0.18	0.89 ± 0.12	7.67 ± 0.28	1.92 ± 0.14	1.94 ± 0.16	4.11 ± 0.15	1.76 ± 0.27	6.67 ± 0.19
P-OF	0.53 ± 0.04	1.75 ± 0.12	1.25 ± 0.06	9.25 ± 0.17	1.44 ± 0.18	1.42 ± 0.20	3.45 ± 0.21	2.54 ± 0.12	6.01 ± 0.12
CH-OF	0.49 ± 0.02	1.69 ± 0.10	1.34 ± 0.08	9.64 ± 0.11	1.32 ± 0.14	1.31 ± 0.12	3.26 ± 0.18	2.59 ± 0.35	5.92 ± 0.13
PCH-OF	0.32 ± 0.03	2.10 ± 0.24	1.72 ± 0.09	10.97 ± 0.19	0.81 ± 0.09	0.77 ± 0.17	2.19 ± 0.22	3.12 ± 0.37	4.76 ± 0.29

* NC= Negative control, PC= Positive control, OF = treated with optimized THYM-NIO, P-OF = treated with PEGylated THYM-NIO, CH-OF = treated with chitosomes and PCH-OF = treated with PEGylated chitosomes.
** Malondialdehyde (MDA), Superoxide dismutase (SOD), Glutathione (GSH), Glutathione peroxidase (GPx), Interleukin-1 beta (IL-1β), Tumor necrosis factor (TNF-α), Amyloid-beta (Aβ), Dopamine (DA) and Glial fibrillary acidic protein (GFAP).

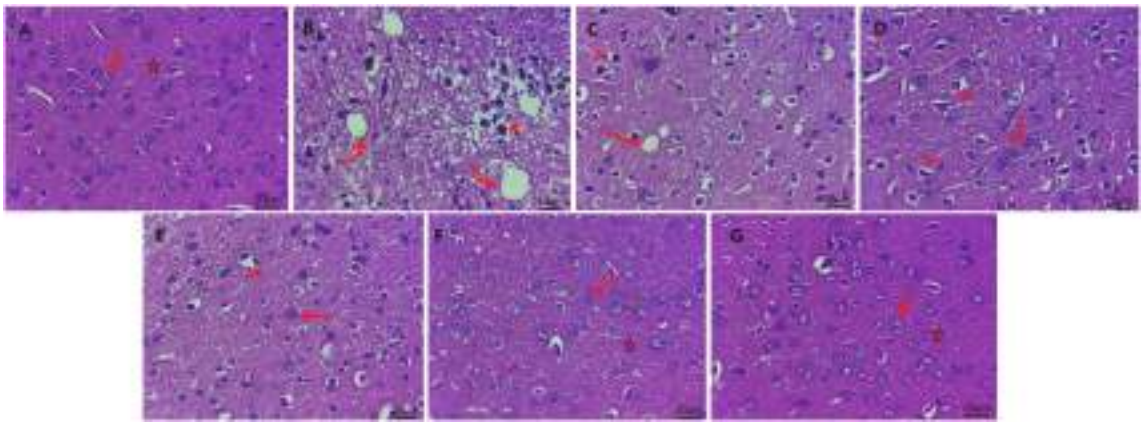

Fig. 9. H&E-stained photomicrographs of the cerebral cortex displaying intact histological architecture, including neurons (arrows), glial cells, neuropil (stars) at Negative control group **(A)**. Abundant numbers of pyknotic neurons surrounded by halo zones (arrowhead) beside presence of large, rounded vacuoles within neuropil (curved arrows) at Positive control group **(B)**. Spongiosis of neuropil (curved arrow), and numbers of pyknotic neurons (arrowhead) at free THYM-treated group **(C)**. Moderate number of Pyknotic neurons (arrowhead), with the few morphologically normal neurons (arrow) in group treated with optimized formula (OF) **(D)**. Normal architectures of most neurons (arrow) with moderate numbers of pyknotic neurons (arrowhead) at group treated with PEGylated THYM-NIO (P-OF) **(E).** THYM-chitosomes treated group revealing aggregation and activation of glial cells around some degenerated neurons (arrows), while most neurons retain normal histological features (stars) **(F)**. Preserved structures of neuronal cell body (arrow), glia cells and neuropil (star) at group treated with PEGylated THYM-chitosomes (PCH-OF) **(G)**.

glial cells. The neuropil displayed a faint eosinophilic background, indicating preserved tissue integrity and absence of pathological alterations. In contrast, the positive $AlCl_3$ induced group (Fig. 9B) showed pronounced histopathological damage. Marked neuronal loss was evident, manifested by large, rounded vacuoles within the neuropil, reflecting severe spongiosis. Numerous pyknotic neurons with condensed, darkly stained nuclei were observed, frequently surrounded by clear perineuronal halo spaces, indicating advanced neuronal degeneration and cytotoxic injury.

The free THYM–treated group, (Fig. 9C), exhibited a mild degree of histological improvement compared to positive control. A noticeable reduction in neuropil spongiosis was observed; however, moderate numbers of pyknotic neurons persisted, indicating incomplete neuroprotection.

The uncoated optimized OF treated group, (Fig. 9D), demonstrated largely preserved histological features of the cerebral cortex. Neurons and glial cells appeared structurally intact, with a faintly eosinophilic neuropil and normal vascular profiles, suggesting a limited protective effect against neurotoxic insult.

Further improvement was evident in the group treated with PEGylated THYM-NIO and THYM-chitosomes, (Fig. 9E and F), which showed near-normal neuronal architecture. They demonstrated moderate neuroprotective effects, as evidenced by the presence of activated glial cells surrounding some degenerated neurons. This gliosis suggests an ongoing reparative or inflammatory response associated with partial neuronal recovery. Most neurons appeared intact with regular morphology, glial cells were randomly and normally distributed, and only occasional pyknotic neurons were detected, reflecting enhanced tissue preservation.

Notably, the double coated formula, PCH-OF, (Fig. 9G), displayed the highest degree of histological amelioration. Brain tissues showed well-preserved neuronal cell bodies, intact glial cell distribution, and a structurally normal neuropil, closely resembling the negative control group. These findings indicate superior neuroprotective efficacy of the mixed coated formulation. Our findings for histopathological examination were in accordance with previous studies [8,147,158].

Overall, the in vitro physicochemical characteristics of the developed nanovesicular systems demonstrate a coherent relationship with the observed in vivo therapeutic outcomes. The optimized nanoscale particle size likely facilitated improved interaction with the blood–brain barrier, while chitosan coating imparted a positive surface charge that may enhance endothelial interaction through adsorptive-mediated mechanisms. Additionally, PEGylation and dual polymer coating contributed to improved entrapment efficiency and sustained release

behavior, which may support prolonged CNS drug availability and reduced burst-associated fluctuations. These combined formulations' attributes contributed to the superior behavioral performance and biochemical modulation observed in the treated groups, including improved cognitive indices and attenuation of oxidative stress markers. The findings therefore suggest a functional correlation between nano-carrier design parameters and therapeutic efficacy in the Alzheimer's disease model.

4. Conclusion

The promising characteristics and stability of the fabricated THYM-NIO and coated THYM-NIO *viz*; small PS, stable ZP, high drug loading capacity, sustained release profile assisted in the ability of THYM brain targeting and improving its efficacy. Yet comprehensive in vivo study on induced-$AlCl_3$ Alzheimer's rats revealed that double coated PEGylated THYM-chitosomes showed the maximum improvement in cognitive functions, oxidative stress as well as neuronal specific biomarkers compared to free THYM solution and uncoated niosomal formulae. The superiority of double coated formula was supported by histopathological examination where specimens showed approximately normal profile. To conclude, PEG/chitosan polymer coating for THMY-NIO probably enables THYM to overcome obstacles for management of Alzheimer's disease.

Ethics approval

The experimental protocol involving animals received ethical clearance from the Research Ethics Committee, Faculty of Pharmacy, Zagazig University (Approval No.: ZU-IACUC/3/F/28/2024). All experimental procedures involving animals were carried out in accordance with the Scientific Procedures Act 1986, and its associated regulations, the EU Directive 2010/63 on the welfare of animals in research, and/or the NIH Guide for the care and use of laboratory animals, or other comparable globally documented guidelines.

Availability of data and materials

Data will be made available on request.

Declaration of generative AI and AI-assisted technologies in the writing process

During the preparation of this work, the authors used QuillBot/Paraphraser (Standard/free version) as little as possible to improve readability and language solely. After using this tool/service, the authors reviewed and edited the content as needed and took full responsibility for the publication's content.

Funding

This research did not receive any specific grant from funding agencies in the public, commercial, or not-for-profit sectors.

CRediT authorship contribution statement

Shaimaa A. Mohamed: Formal analysis, Investigation, Methodology, Software, Validation, Writing – original draft. **Eman Gomaa:** Data curation, Formal analysis, Supervision, Visualization, Writing – review & editing. **Hanaa A. Elghamry:** Conceptualization, Resources, Supervision, Visualization, Writing – review & editing. **Esraa M. Fahmy:** Data curation, Investigation, Methodology, Resources, Visualization. **Asmaa I. Abdelaty:** Data curation, Investigation, Methodology, Resources, Visualization. **Mohamed A. Megahed:** Conceptualization, Data curation, Formal analysis, Software, Supervision, Validation, Visualization, Writing – review & editing.

Declaration of competing interest

The authors declare that they have no known competing financial interests or personal relationships that could have appeared to influence the work reported in this paper.

Appendix A. Supplementary data

Supplementary data to this article can be found online at https://doi.org/10.1016/j.jddst.2026.108370.

Data availability

Data will be made available on request.

References

[1] J. Emerit, M. Edeas, F. Bricaire, Neurodegenerative diseases and oxidative stress, Biomed. Pharmacother. 58 (1) (2004) 39–46, https://doi.org/10.1016/j.biopha.2003.11.004.
[2] S.K. Shahbaz, K. Koushki, T. Sathyapalan, M. Majeed, A. Sahebkar, PLGA-Based curcumin delivery System: an interesting therapeutic approach in the treatment of alzheimer's disease, Curr. Neuropharmacol. 20 (2) (2022) 309–323, https://doi.org/10.2174/1570159x19666210823103020.
[3] M. Asadbegi, A. Komaki, I. Salehi, P. Yaghmaei, A. Ebrahim-Habibi, S. Shahidi, A. Sarihi, S.S. Asl, Z. Golipoor, Effects of thymol on amyloid-β-induced impairments in hippocampal synaptic plasticity in rats fed a high-fat diet, Brain Res. Bull. 137 (2018) 338–350, https://doi.org/10.1016/j.brainresbull.2018.01.008.
[4] Y. Ju, K. Tam, Pathological mechanisms and therapeutic strategies for Alzheimer's disease, Neural Regen. Res. 17 (3) (2022) 543–549, https://doi.org/10.4103/1673-5374.320970.
[5] B. Anand, Q. Wu, M. Nakhaei-Nejad, G. Karthivashan, L. Dorosh, S. Amidian, A. Dahal, X. Li, M. Stepanova, H. Wille, F. Giuliani, S. Kar, Significance of native PLGA nanoparticles in the treatment of Alzheimer's disease pathology, Bioact. Mater. 17 (2022) 506–525, https://doi.org/10.1016/j.bioactmat.2022.05.030.
[6] C.M. Karch, A.M. Goate, Alzheimer's disease risk genes and mechanisms of disease pathogenesis, Biol. Psychiatry 77 (1) (2015) 43–51, https://doi.org/10.1016/j.biopsych.2014.05.006.
[7] K.M. Heilman, S.E. Nadeau, Emotional and neuropsychiatric disorders associated with alzheimer's disease, Neurotherapeutics 19 (1) (2022) 99–116, https://doi.org/10.1007/s13311-021-01172-w.
[8] A.M.E. Hamdan, F.H.J. Alharthi, A.H. Alanazi, S.Z. El-Emam, S.S. Zaghlool, K. Metwally, S.A. Albalawi, Y.S. Abdu, R.E.S. Mansour, H.A. Salem, Z.Y. Abd Elmageed, K. Abu-Elfotuh, Neuroprotective effects of phytochemicals against Aluminum chloride-induced alzheimer's disease through ApoE4/LRP1, Wnt3/β-Catenin/GSK3β, and TLR4/NLRP3 pathways with physical and mental activities in a rat model, Pharmaceuticals 15 (8) (2022) 1008, https://doi.org/10.3390/ph15081008.
[9] J. Venugopalan, L. Tong, H.R. Hassanzadeh, M.D. Wang, Multimodal deep learning models for early detection of Alzheimer's disease stage, Sci. Rep. 11 (2021) 3245, https://doi.org/10.1038/s41598-020-74399-w.
[10] P. Krashia, A. Nobili, M. D'Amelio, Unifying Hypothesis of dopamine neuron loss in neurodegenerative diseases: focusing on alzheimer's disease, Front. Mol. Neurosci. 12 (2019) 123, https://doi.org/10.3389/fnmol.2019.00123.
[11] M.A. Korolainen, S. Auriola, T.A. Nyman, I. Alafuzoff, T. Pirttilä, Proteomic analysis of glial fibrillary acidic protein in Alzheimer's disease and aging brain, Neurobiol. Dis. 20 (3) (2005) 858–870, https://doi.org/10.1016/j.nbd.2005.05.021.
[12] C. Venkateshappa, G. Harish, A. Mahadevan, M.M. Srinivas Bharath, S. K. Shankar, Elevated oxidative stress and decreased antioxidant function in the human Hippocampus and frontal cortex with increasing Age: implications for neurodegeneration in alzheimer's disease, Neurochem. Res. 37 (8) (2012) 1601–1614, https://doi.org/10.1007/s11064-012-0755-8.
[13] G. Azizi, A. Mirshafiey, The potential role of proinflammatory and antiinflammatory cytokines in Alzheimer's disease pathogenesis, Immunopharmacol. Immunotoxicol. 34 (6) (2012) 881–895, https://doi.org/10.3109/08923973.2012.705292.
[14] M.C. Morris, C.C. Tangney, Dietary fat composition and dementia risk, Neurobiol. Aging 35 (Suppl. 2) (2014) S59–S64, https://doi.org/10.1016/j.neurobiolaging.2014.03.038.
[15] S. Rivas-Arancibia, L.F.H. Zimbrón, E. Rodríguez-Martínez, P.D. Maldonado, G. Borgonio Pérez, M. Sepúlveda-Parada, Oxidative stress-dependent changes in immune responses and cell death in the substantia nigra after ozone exposure in rat, Front. Aging Neurosci. 7 (2015) 65, https://doi.org/10.3389/fnagi.2015.00065.
[16] T.M. Saber, A.M.A. Abo-Elmaaty, E.N. Said, R.R. Beheiry, A.A.A. Moselhy, F. E. Abdelgawad, M.H. Arisha, T. Saber, A.H. Arisha, E.M. Fahmy, Alhagi maurorum ethanolic extract rescues hepato-neurotoxicity and neurobehavioral alterations induced by lead in rats via abrogating oxidative stress and the

Caspase-3-Dependent apoptotic pathway, Antioxidants 11 (10) (2022) 1992, https://doi.org/10.3390/antiox11101992.
[17] M. Asadbegi, P. Yaghmaei, I. Salehi, A. Komaki, A. Ebrahim-Habibi, Investigation of thymol effect on learning and memory impairment induced by intrahippocampal injection of amyloid beta peptide in high fat diet-fed rats, Metab. Brain Dis. 32 (2017) 827–839, https://doi.org/10.1007/s11011-017-9960-0.
[18] N.V. Yanishlieva, E.M. Marinova, M.H. Gordon, V.G. Raneva, Antioxidant activity and mechanism of action of thymol and carvacrol in two lipid systems, Food Chem. 64 (1) (1999) 59–66, https://doi.org/10.1016/S0308-8146(98)00086-7.
[19] P.C. Braga, M. Dal Sasso, M. Culici, T. Bianchi, L. Bordoni, L. Marabini, Anti-inflammatory activity of thymol: inhibitory effect on the release of human neutrophil Elastase, Pharmacology 77 (3) (2006) 130–136, https://doi.org/10.1159/000093790.
[20] J. Sheorain, M. Mehra, R. Thakur, S. Grewal, S. Kumari, In vitro anti-inflammatory and antioxidant potential of thymol loaded bipolymeric (tragacanth gum/chitosan) nanocarrier, Int. J. Biol. Macromol. 125 (2019) 1069–1074, https://doi.org/10.1016/j.ijbiomac.2018.12.095.
[21] FangFang, H. Li, T. Qin, M. Li, S. Ma, Thymol improves high-fat diet-induced cognitive deficits in mice via ameliorating brain insulin resistance and upregulating NRF2/HO-1 pathway, Metab. Brain Dis. 32 (2) (2017) 385–393, https://doi.org/10.1007/s11011-016-9921-z.
[22] H. Javed, S. Azimullah, M.N. Meeran, S.A. Ansari, S. Ojha, Neuroprotective effects of Thymol, a dietary monoterpene against dopaminergic neurodegeneration in rotenone-induced rat model of parkinson's disease, Int. J. Mol. Sci. 20 (7) (2019) 1538, https://doi.org/10.3390/ijms20071538.
[23] M.R. Loizzo, F. Menichini, F. Conforti, R. Tundis, M. Bonesi, A.M. Saab, G. A. Statti, B. de Cindio, P.J. Houghton, F. Menichini, N.G. Frega, Chemical analysis, antioxidant, antiinflammatory and anticholinesterase activities of Origanum ehrenbergii Boiss and Origanum syriacum L. essential oils, Food Chem. 117 (1) (2009) 174–180, https://doi.org/10.1016/j.foodchem.2009.03.095.
[24] M. Öztürk, Anticholinesterase and antioxidant activities of Savoury (*Satureja thymbra L.*) with identified major terpenes of the essential oil, Food Chem. 134 (1) (2012) 48–54, https://doi.org/10.1016/j.foodchem.2012.02.054.
[25] A.K. Singhal, V. Naithani, O.P. Bangar, Medicinal plants with a potential to treat Alzheimer and associated symptoms, Int. J. Nutr. Pharmacol. Neurol. Dis. 2 (2) (2012) 84–91, https://doi.org/10.4103/2231-0738.95927.
[26] S. Saravanan, L. Pari, Role of thymol on hyperglycemia and hyperlipidemia in high fat diet-induced type 2 diabetic C57BL/6J mice, Eur. J. Pharmacol. 761 (2015) 279–287, https://doi.org/10.1016/j.ejphar.2015.05.034.
[27] M.F. Nagoor Meeran, H. Javed, H. Al Taee, S. Azimullah, S.K. Ojha, Pharmacological properties and molecular mechanisms of thymol: prospects for its therapeutic potential and pharmaceutical development, Front. Pharmacol. 8 (2017) 380, https://doi.org/10.3389/fphar.2017.00380.
[28] W. Zhou, Y. Zhang, R. Li, S. Peng, R. Ruan, J. Li, W. Liu, Fabrication of caseinate stabilized Thymol nanosuspensions via the pH-Driven method: enhancement in water solubility of Thymol, Foods 10 (5) (2021) 1074, https://doi.org/10.3390/foods10051074.
[29] M. Bragagni, N. Mennini, S. Furlanetto, S. Orlandini, C. Ghelardini, P. Mura, Development and characterization of functionalized niosomes for brain targeting of dynorphin-B, Eur. J. Pharm. Biopharm. 87 (1) (2014) 73–79, https://doi.org/10.1016/j.ejpb.2014.01.006.
[30] I.F. Uchegbu, S.P. Vyas, Non-ionic surfactant based vesicles (niosomes) in drug delivery, Int. J. Pharm. 172 (1–2) (1998) 33–70, https://doi.org/10.1016/S0378-5173(98)00169-0.
[31] M. Mészáros, G. Porkoláb, L. Kiss, A.-M. Pilbat, Z. Kóta, Z. Kupihár, A. Kéri, G. Galbács, L. Siklós, A. Tóth, L. Fülöp, M. Csete, Á. Sipos, P. Hülper, P. Sipos, T. Páli, G. Rákhely, P. Szabó-Révész, M.A. Deli, S. Veszelka, Niosomes decorated with dual ligands targeting brain endothelial transporters increase cargo penetration across the blood-brain barrier, Eur. J. Pharmaceut. Sci. 123 (2018) 228–240, https://doi.org/10.1016/j.ejps.2018.07.042.
[32] Y. Aktaş, M. Yemisci, K. Andrieux, R.N. Gürsoy, M.J. Alonso, E. Fernandez-Megia, R. Novoa-Carballal, E. Quiñoá, R. Riguera, M.F. Sargon, H.H. Çelik, A.S. Demir, A. A. Hincal, T. Dalkara, Y. Çapan, P. Couvreur, Development and brain delivery of Chitosan-PEG nanoparticles functionalized with the monoclonal antibody OX26, Bioconjug. Chem. 16 (6) (2005) 1503–1511, https://doi.org/10.1021/bc050217o.
[33] Z. Cui, R.J. Mumper, Chitosan-based nanoparticles for topical genetic immunization, J. Contr. Release 75 (3) (2001) 409–419, https://doi.org/10.1016/S0168-3659(01)00407-2.
[34] N. Ahmad, Rasagiline-encapsulated chitosan-coated PLGA nanoparticles targeted to the brain in the treatment of Parkinson's disease, J. Liq. Chromatogr. Relat. Technol. 40 (13) (2017) 677–690, https://doi.org/10.1080/10826076.2017.1343735.
[35] N. Ahmad, R. Ahmad, A.A. Naqvi, M.A. Alam, M. Ashafaq, M. Samim, Z. Iqbal, F. J. Ahmad, Rutin-encapsulated chitosan nanoparticles targeted to the brain in the treatment of Cerebral Ischemia, Int. J. Biol. Macromol. 91 (2016) 640–655, https://doi.org/10.1016/j.ijbiomac.2016.06.001.
[36] M.M. Badran, M.M. Mady, M.M. Ghannam, F. Shakeel, Preparation and characterization of polymeric nanoparticles surface modified with chitosan for target treatment of colorectal cancer, Int. J. Biol. Macromol. 95 (2017) 643–649, https://doi.org/10.1016/j.ijbiomac.2016.11.098.
[37] A.E. Caprifico, P.J.S. Foot, E. Polycarpou, G. Calabrese, Overcoming the blood-brain barrier: functionalised chitosan nanocarriers, Pharmaceutics 12 (11) (2020) 1013, https://doi.org/10.3390/pharmaceutics12111013.
[38] H. Cortés, S. Alcalá-Alcalá, I.H. Caballero-Florán, S.A. Bernal-Chávez, A. Ávalos-Fuentes, M. González-Torres, M.G. Del Carmen, G. Figueroa-González, O. D. Reyes-Hernández, B. Floran, M.L.D. Prado-Audelo, G. Leyva-Gómez, A reevaluation of Chitosan-Decorated nanoparticles to cross the blood-brain barrier, Membranes 10 (9) (2020) 212, https://doi.org/10.3390/membranes10090212.
[39] A. Trapani, E. De Giglio, D. Cafagna, N. Denora, G. Agrimi, T. Cassano, S. Gaetani, V. Cuomo, G. Trapani, Characterization and evaluation of chitosan nanoparticles for dopamine brain delivery, Int. J. Pharm. 419 (1–2) (2011) 296–307, https://doi.org/10.1016/j.ijpharm.2011.07.036.
[40] N. Ahmad, R. Ahmad, M.A. Alam, F.J. Ahmad, Quantification and brain targeting of eugenol-loaded surface modified nanoparticles through intranasal route in the treatment of cerebral ischemia, Drug Res. 68 (10) (2018) 584–595, https://doi.org/10.1055/a-0596-7288.
[41] Y.C. Kuo, L.J. Wang, R. Rajesh, Targeting human brain cancer stem cells by curcumin-loaded nanoparticles grafted with anti-aldehyde dehydrogenase and sialic acid: colocalization of ALDH and CD44, Mater. Sci. Eng. C 102 (2019) 362–372, https://doi.org/10.1016/j.msec.2019.04.065.
[42] M. Saeedi, M. Eslamifar, K. Khezri, S.M. Dizaj, Applications of nanotechnology in drug delivery to the central nervous system, Biomed. Pharmacother. 111 (2019) 666–675, https://doi.org/10.1016/j.biopha.2018.12.133.
[43] X. Zheng, X. Shao, C. Zhang, Y. Tan, Q. Liu, X. Wan, Q. Zhang, S. Xu, X. Jiang, Intranasal H102 peptide-loaded liposomes for brain delivery to treat alzheimer's disease, Pharm. Res. 32 (2015) 3837–3849, https://doi.org/10.1007/s11095-015-1744-9.
[44] I. Brigger, J. Morizet, G. Aubert, H. Chacun, M. Terrier-Lacombe, P. Couvreur, G. Vassal, Poly(ethylene glycol)-coated hexadecylcyanoacrylate nanospheres display a combined effect for brain tumor targeting, J. Pharmacol. Exp. Therapeut. 303 (3) (2002) 928–936, https://doi.org/10.1124/jpet.102.039669.
[45] E.A. Nance, G.F. Woodworth, K.A. Sailor, T.Y. Shih, Q. Xu, G. Swaminathan, D. Xiang, C. Eberhart, J. Hanes, A dense poly(ethylene glycol) coating improves penetration of large polymeric nanoparticles within brain tissue, Sci. Transl. Med. 4 (149) (2012) 149ra119, https://doi.org/10.1126/scitranslmed.3003594.
[46] Y. Sheng, C. Liu, Y. Yuan, X. Tao, F. Yang, X. Shan, H. Zhou, F. Xu, Long-circulating polymeric nanoparticles bearing a combinatorial coating of PEG and water-soluble chitosan, Biomaterials 30 (12) (2009) 2340–2348, https://doi.org/10.1016/j.biomaterials.2008.12.070.
[47] A. Cimini, B. D'angelo, S. Das, R. Gentile, E. Benedetti, V. Singh, A.M. Monaco, S. Santucci, S. Seal, Antibody-conjugated PEGylated cerium oxide nanoparticles for specific targeting of Aβ aggregates modulate neuronal survival pathways, Acta Biomater. 8 (6) (2012) 2056–2067, https://doi.org/10.1016/j.actbio.2012.01.035.
[48] W. Li, J. Wu, J. Liu, J. Wang, D. Xiang, S. Luo, X. Liu, Puerarin-loaded PEG-PE micelles with enhanced anti-apoptotic effect and better pharmacokinetic profile, Drug Deliv. 25 (1) (2018) 827–837, https://doi.org/10.1080/10717544.2018.1455763.
[49] S.Y. Fam, C.F. Chee, C.Y. Yong, K.L. Ho, A.R. Mariatulqabtiah, W.S. Tan, Stealth coating of nanoparticles in drug-delivery systems, Nanomaterials 10 (4) (2020) 787, https://doi.org/10.3390/nano10040787.
[50] M. Vishwakarma, P. Agrawal, S. Soni, S. Tomar, T. Haider, S.K. Kashaw, V. Soni, Cationic nanocarriers: a potential approach for targeting negatively charged cancer cell, Adv. Colloid Interface Sci. 327 (2024) 103160, https://doi.org/10.1016/j.cis.2024.103160.
[51] Y. Deng, B. Li, H. Zheng, L. Liang, Y. Yang, S. Liu, M. Wang, C. Peng, B. Liu, W. Wang, H. Yu, Multifunctional Prussian blue nanoparticles loading Xuetongsu for efficient rheumatoid arthritis therapy through targeting inflammatory macrophages and osteoclasts, Asian J. Pharm. Sci. 20 (2025) 101037, https://doi.org/10.1016/j.ajps.2025.101037.
[52] H. Wang, C. Tang, Y. Xiang, C. Zou, J. Hu, G. Yang, W. Zhou, Tea polyphenol-derived nanomedicine for targeted photothermal thrombolysis and inflammation suppression, J. Nanobiotechnol. 22 (2024) 146, https://doi.org/10.1186/s12951-024-02446-z.
[53] M.A. Ali, M.I. Mohamed, M.A. Megahed, T.M. Abdelghany, K.M. El-Say, Cholesterol-Based nanovesicles enhance the in vitro cytotoxicity, Ex vivo intestinal absorption, and in vivo bioavailability of flutamide, Pharmaceutics 13 (11) (2021) 1741, https://doi.org/10.3390/pharmaceutics13111741.
[54] K.M. El-Say, F.I. Abd-Allah, A.E. Lila, A.E.S.A. Hassan, A.E.A. Kassem, Diacerein niosomal gel for topical delivery: development, in vitro and in vivo assessment, J. Liposome Res. 26 (1) (2016) 57–68, https://doi.org/10.3109/08982104.2015.1029495.
[55] M.A. Kassem, M.A. Megahed, S.K. Abu Elyazid, F.I. Abd-Allah, T.M. Abdelghany, A.M. Al-Abd, K.M. El-Say, Enhancing the therapeutic efficacy of Tamoxifen citrate loaded span-based nano-vesicles on human breast adenocarcinoma cells, AAPS PharmSciTech 19 (2018) 1529–1543, https://doi.org/10.1208/s12249-018-0962-y.
[56] M.S. El-Ridy, A. Abdelbary, T. Essam, R.M. Abd El-Salam, A.A. Aly Kassem, Niosomes as a potential drug delivery system for increasing the efficacy and safety of nystatin, Drug Dev. Ind. Pharm. 37 (12) (2011) 1491–1508, https://doi.org/10.3109/03639045.2011.587431.
[57] S. Amirkhanloo, R. Enayatifard, J. Akbari, M. Seyedabadi, M. Saeedi, M. Ranaee, Vanillic acid-loaded niosomes for diabetic wound healing: formulation, optimization by box–behnken design, and in vivo evaluation, AAPS PharmSciTech 27 (2026) 62, https://doi.org/10.1208/s12249-025-03249-7.
[58] M.G. Arafa, B.M. Ayoub, DOE optimization of nano-based carrier of Pregabalin as Hydrogel: new therapeutic & chemometric approaches for controlled drug delivery systems, Sci. Rep. 7 (2017) 41503, https://doi.org/10.1038/srep41503.

[59] M.A. Luthfi, I.T. Husna, S. Dahlizar, Y. Meliana, A.W. Septama, Innovative niosome Gel loaded *Curcuma Xanthorrhiza* extract: development formulation, characterization, and evaluation of their antibacterial activity, J. Pharm. Innov. 21 (2026) 28, https://doi.org/10.1007/s12247-025-10260-9.
[60] Y. Hao, F. Zhao, N. Li, Y. Yang, K. Li, Studies on a high encapsulation of colchicine by a niosome system, Int. J. Pharm. 244 (1–2) (2002) 73–80, https://doi.org/10.1016/s0378-5173(02)00301-0.
[61] R.A. Khallaf, H.M. Aboud, O.M. Sayed, Surface modified niosomes of olanzapine for brain targeting via nasal route; preparation, optimization, and *in vivo* evaluation, J. Liposome Res. 30 (2) (2020) 163–173, https://doi.org/10.1080/08982104.2019.1610435.
[62] A. Manosroi, P. Wongtrakul, J. Manosroi, H. Sakai, F. Sugawara, M. Yuasa, M. Abe, Characterization of vesicles prepared with various non-ionic surfactants mixed with cholesterol, Colloids Surf. B Biointerfaces 30 (1–2) (2003) 129–138, https://doi.org/10.1016/S0927-7765(03)00080-8.
[63] S. Yeom, B.S. Shin, S. Han, An electron spin resonance study of non-ionic surfactant vesicles (niosomes), Chem. Phys. Lipids 181 (2014) 83–89, https://doi.org/10.1016/j.chemphyslip.2014.03.004.
[64] L.M. Ahmed, F.A. Mohamed, T.H. Elfaham, Nanocrystals as a promising approach for enhancing solubility and dissolution of etoricoxib using Box–Behnken design, Sci. Rep. 15 (2025) 29347, https://doi.org/10.1038/s41598-025-12837-3.
[65] T. Andersen, Ž. Vanić, G. Eide Flaten, S. Mattsson, I. Tho, N. Škalko-Basnet, Pectosomes and chitosomes as delivery systems for metronidazole: the one-pot preparation method, Pharmaceutics 5 (3) (2013) 445–456, https://doi.org/10.3390/pharmaceutics5030445.
[66] M.A. Megahed, H.S. El-Sawy, A.M. Reda, F.I. Abd-Allah, S.K. Abu Elyazid, A. E. Lila, H.R. Ismael, K.M. El-Say, Effect of nanovesicular surface-functionalization via chitosan and/or PEGylation on cytotoxicity of tamoxifen in induced-breast cancer model, Life Sci. 307 (2022) 120908, https://doi.org/10.1016/j.lfs.2022.120908.
[67] S.K. Shukla, A. Chan, V. Parvathaneni, V. Gupta, Metformin-loaded chitosomes for treatment of malignant pleural mesothelioma – a rare thoracic cancer, Int. J. Biol. Macromol. 160 (2020) 128–141, https://doi.org/10.1016/j.ijbiomac.2020.05.146.
[68] G.M. El-Zaafarany, M.E. Soliman, S. Mansour, G.A.S. Awad, Identifying lipidic emulsomes for improved oxcarbazepine brain targeting: in vitro and rat in vivo studies, Int. J. Pharm. 503 (1–2) (2016) 127–140, https://doi.org/10.1016/j.ijpharm.2016.02.038.
[69] X. Zhou, Z. Chen, Preparation and performance evaluation of emulsomes as a drug delivery system for silybin, Arch Pharm. Res. (Seoul) 38 (2015) 2193–2200, https://doi.org/10.1007/s12272-015-0630-7.
[70] H. Hajimehdipoor, M. Shekarchi, M. Khanavi, N. Adib, M. Amri, A validated high performance liquid chromatography method for the analysis of thymol and carvacrol in Thymus vulgaris L. volatile oil, Pharmacogn. Mag. 6 (23) (2010) 154–158, https://doi.org/10.4103/0973-1296.66927.
[71] A.K. Chettupalli, S.P.N. Bukke, S. Abdul Rahaman, M. Bodige, V.K. Kanakaraju, M. Kavitha, D. Srinivasarao, A. Mohammed, N. Goruntla, T.M. Yadesa, Design, optimization of Niosomal gel capability for solubility and bioavailability enhancement of Kynurenic acid after intranasal administration: in Vitro and in Vivo Evaluation, BMC Biotechnol. 25 (2025) 134, https://doi.org/10.1186/s12896-025-01069-y.
[72] R.A. Radi, M.A. Kandeil, E.T. Mohammed, M.A. Ibrahim, A. Gamal, A.H. Abdel-Razik, F. Khalil, D. Sabry, Neuroprotective effects of Chlorella vulgaris loaded niosomes via SIRT1 activation in aluminum chloride-induced Alzheimer's model, Sci. Rep. 15 (1) (2025) 40361, https://doi.org/10.1038/s41598-025-25892-7.
[73] D.S. Shaker, M.A. Shaker, M.S. Hanafy, Cellular uptake, cytotoxicity and in-vivo evaluation of Tamoxifen citrate loaded niosomes, Int. J. Pharm. 493 (1–2) (2015) 285–294, https://doi.org/10.1016/j.ijpharm.2015.07.041.
[74] M.A. Altamimi, A. Hussain, M. Alrajhi, S. Alshehri, S.S. Imam, W. Qamar, Luteolin-Loaded elastic liposomes for transdermal delivery to control breast cancer: in vitro and Ex vivo evaluations, Pharmaceuticals 14 (11) (2021) 1143, https://doi.org/10.3390/ph14111143.
[75] D.S. Shaker, M.A. Shaker, A. Klingner, M.S. Hanafy, In situ thermosensitive Tamoxifen citrate loaded hydrogels: an effective tool in breast cancer loco-regional therapy, J. Drug Deliv. Sci. Technol. 35 (2016) 155–164, https://doi.org/10.1016/j.jddst.2016.05.007.
[76] M. Zewail, P.M.E. Gaafar, M.M. Ali, H. Abbas, Lipidic cubic-phase leflunomide nanoparticles (cubosomes) as a potential tool for breast cancer management, Drug Deliv. 29 (1) (2022) 1663–1674, https://doi.org/10.1080/10717544.2022.2079770.
[77] Y.L. Youssef, M.A. Megahed, G.M. El-Zaafarany, R. Osman, Emulsomal nanovesicles: a platform for boosting the oral bioavailability and selective cytotoxicity of tamoxifen citrate towards breast cancer cells, J. Drug Deliv. Sci. Technol. 108 (2025) 106897, https://doi.org/10.1016/j.jddst.2025.106897.
[78] G. Karan, A. Pradhan, S.K. Dey, S. Manna, R. Mahata, A. Das Choudhuri, D. Giri, P. Maity, M. Bepari, A.K. Das, S. Maiti Choudhury, Comprehensive and comparative analysis of sorbitan ester (Span) niosomes as emerging vesicular drug delivery platforms: fabrication, characterization, release dynamics, biocompatibility profiling, and toxicological implications, Colloids Surf. A Physicochem. Eng. Asp. 728 (2026) 138731, https://doi.org/10.1016/j.colsurfa.2025.138731.
[79] A. Miatmoko, S.A. Safitri, F. Aquila, D.M. Cahyani, B.S. Hariawan, E. Hendrianto, E. Hendradi, R. Sari, Characterization and distribution of niosomes containing ursolic acid coated with chitosan layer, Res. Pharm. Sci. 16 (6) (2021) 660–673, https://doi.org/10.4103/1735-5362.327512.
[80] S. Moghassemi, A. Hadjizadeh, Nano-niosomes as nanoscale drug delivery systems: an illustrated review, J. Contr. Release 185 (2014) 22–36, https://doi.org/10.1016/j.jconrel.2014.04.015.
[81] M.F. Zaky, T.M. Hammady, S. Gad, A. Alattar, R. Alshaman, A. Hegazy, S. A. Zaitone, M.M. Ghorab, M.A. Megahed, Influence of surface-modification via PEGylation or chitosanization of lipidic nanocarriers on in vivo Pharmacokinetic/Pharmacodynamic profiles of Apixaban, Pharmaceutics 15 (6) (2023) 1668, https://doi.org/10.3390/pharmaceutics15061668.
[82] M.F. Zaky, M.A. Megahed, T.M. Hammady, S. Gad, M.M. Ghorab, K.M. El-Say, Tailoring apixaban in nanostructured lipid carrier enhancing its oral bioavailability and anticoagulant activity, Pharmaceutics 15 (1) (2023) 80, https://doi.org/10.3390/pharmaceutics15010080.
[83] H.H. Awad, M.A. Desouky, A. Zidan, M. Bassem, A. Qasem, M. Farouk, H. AlDeab, M. Fouad, C. Hany, N. Basem, R. Nader, A. Alkalleny, V. Reda, M.Y. George, Neuromodulatory effect of vardenafil on aluminium chloride/D-galactose induced Alzheimer's disease in rats: emphasis on amyloid-beta, p-tau, PI3K/Akt/p53 pathway, endoplasmic reticulum stress, and cellular senescence, Inflammopharmacology 31 (5) (2023) 2653–2673, https://doi.org/10.1007/s10787-023-01287-w.
[84] S. Elshamy, A. Abdel Motaal, M. Abdel-Halim, D. Medhat, H. Handoussa, Potential neuroprotective activity of Mentha longifolia L. in aluminum chloride-induced rat model of Alzheimer's disease, J. Food Biochem. 45 (4) (2021) e13644, https://doi.org/10.1111/jfbc.13644.
[85] Y. Hu, X. Fang, J. Wang, T.T. Ren, Y.Y. Zhao, J.F. Dai, X.Y. Qin, R. Lan, Astragalin attenuates $AlCl_3$/D-galactose-induced aging-like disorders by inhibiting oxidative stress and neuroinflammation, Neurotoxicology 91 (2022) 60–68, https://doi.org/10.1016/j.neuro.2022.05.003.
[86] J. Wu, B. Bie, M. Naguib, Epigenetic manipulation of brain-derived neurotrophic factor improves memory deficiency induced by neonatal Anesthesia in rats, Anesthesiology 124 (3) (2016) 624–640, https://doi.org/10.1097/ALN.0000000000000981.
[87] M.A.F. Zaher, M.A. Bendary, A.S. Aly, Effect of thymoquinone against Aluminum chloride-induced alzheimer-like model in rats: a neurophysiological and behavioral Study, Med. J. Cairo Univ. 88 (1) (2020) 355–365, https://doi.org/10.21608/mjcu.2020.93997.
[88] J.M. Snyder, E. Radaelli, A. Goeken, T. Businga, A.W. Boyden, N.J. Karandikar, K. N. Gibson-Corley, Perfusion with 10% neutral-buffered formalin is equivalent to 4% paraformaldehyde for histopathology and immunohistochemistry in a mouse model of experimental autoimmune encephalomyelitis, Vet. Pathol. 59 (3) (2022) 498–505, https://doi.org/10.1177/03009858221075588.
[89] F. Faradila, Y. Syafrita, N.I. Lipoeto, Relationship between amyloid-beta 42 levels and Y-maze alternation values in Sprague Dawley Alzheimer's induction received medium-chain triglycerides therapy, Open Access Maced. J. Med. Sci. 8 (2020) 476–480, https://doi.org/10.3889/OAMJMS.2020.3243.
[90] H. Zhang, L. Wang, Y. Yang, C. Cai, X. Wang, L. Deng, W. Zhou, B. He, Y. Cui, DL-3-n-butylphthalide alleviates post-stroke cognitive impairment by suppressing neuroinflammation and oxidative stress, Front. Pharmacol. 13 (2022) 987293, https://doi.org/10.3389/fphar.2022.987293.
[91] M.Y. George, M.O. El-Derany, Y. Ahmed, M. Zaher, C. Ibrahim, H. Waleed, H. Khaled, G. Khaled, A. Saleh, H. Alshafei, R. Alshafei, N. Ahmed, S. Ezz, N. Ashraf, S.S. Ibrahim, Design and evaluation of chrysin-loaded nanoemulsion against lithium/pilocarpine-induced status epilepticus in rats; emphasis on formulation, neuronal excitotoxicity, oxidative stress, microglia polarization, and AMPK/SIRT-1/PGC-1α pathway, Expert Opin. Drug Deliv. 20 (1) (2023) 159–174, https://doi.org/10.1080/17425247.2023.2153831.
[92] L. Raveh, B.A. Weissman, G. Cohen, D. Alkalay, I. Rabinovitz, H. Sonego, R. Brandeis, Caramiphen and scopolamine prevent soman-induced brain damage and cognitive dysfunction, Neurotoxicology 23 (1) (2002) 7–17, https://doi.org/10.1016/S0161-813X(02)00005-0.
[93] M.I.G. El-Din, M.Y. George, F.S. Youssef, Chemical characterization of the polyphenolic rich fraction of Thunbergia erecta and its therapeutic potential against doxorubicin and cyclophosphamide-induced cognitive impairment in rats, J. Ethnopharmacol. 307 (2023) 116213, https://doi.org/10.1016/j.jep.2023.116213.
[94] S. Li, D. Wang, A. Li, T. Wang, X. Chen, H. Li, T. Wang, Y. Xie, J. Liang, X. Cai, ZuoGui pill ameliorates alzheimer's disease-like pathology in 3xTg-AD mice by targeting Aβ production, Tau phosphorylation, synaptic loss, and neuroinflammation, Mol. Neurobiol. 63 (2026) 96, https://doi.org/10.1007/s12035-025-05336-z.
[95] A.M. Afify, E.K. El-sayed, A. Ismail, S. Nofal, Nanocarrier-enhanced simvastatin modulates AMPK-ULK1 pathway and oxidative stress in Alzheimer's disease model, Eur. J. Pharmacol. 1010 (2026) 178411, https://doi.org/10.1016/j.ejphar.2025.178411.
[96] M.A. Elbaset, B.M.S.A. Mohamed, P.E. Moustafa, T. Esatbeyoglu, S.M. Afifi, A. F. Hessin, S.S. Abdelrahman, H.M. Fayed, Renoprotective effect of pitavastatin against TAA-Induced renal injury: involvement of the miR-93/PTEN/AKT/mTOR pathway, Adv. Pharmacol. Pharm. Sci. 2024 (1) (2024) 6681873, https://doi.org/10.1155/2024/6681873.
[97] K. Kessas, W. Lounis, Z. Chouari, A. Vejux, G. Lizard, O. Kharoubi, Benefits of rutin on mitochondrial function and inflammation in an aluminum-induced neurotoxicity rat model: potential interest for the prevention of neurodegeneration, Biochimie 222 (2024) 1–8, https://doi.org/10.1016/j.biochi.2024.02.010.
[98] M. Sajad, R. Ali, R. Kumar, N.J. Khan, S. Wahab, S.A. Alshehri, S.C. Thakur, Therapeutic potential of cedrol in alleviating cognitive impairments in aluminum

chloride-induced Alzheimer's disease: a biomarker-based approach, Results Chem. 16 (2025) 102487, https://doi.org/10.1016/j.rechem.2025.102487.
[99] R. Kumar, R. Kumar, N. Khurana, S.K. Singh, S. Khurana, S. Verma, N. Sharma, M. Vyas, K. Dua, R. Khursheed, A. Awasthi, S. Vishwas, Improved neuroprotective activity of Fisetin through SNEDDS in ameliorating the behavioral alterations produced in rotenone-induced Parkinson's model, Environ. Sci. Pollut. Res. 29 (2022) 50488–50499, https://doi.org/10.1007/s11356-022-19428-z.
[100] S. Vishwas, R. Kumar, A. Awasthi, L. Corrie, B. Bashir, R. Khursheed, A. K. Ramanunny, Hardeep, M. Gulati, T.G. Singh, G. Cupta, H. Dureja, P. Kumar, A. Alam, K. Dua, S.K. Singh, Formulation and optimization of fisetin nanoemulsion for the treatment of Alzheimer's disease in rats: pharmacokinetic and pharmacodynamic assessment, J. Drug Deliv. Sci. Technol. 101 (2024) 106269, https://doi.org/10.1016/j.jddst.2024.106269.
[101] S. Paciotti, F.N. Sepe, P. Eusebi, L. Farotti, S. Cataldi, L. Gatticchi, L. Parnetti, Diagnostic performance of a fully automated chemiluminescent enzyme immunoassay for Alzheimer's disease diagnosis, Clin. Chim. Acta 494 (2019) 74–78, https://doi.org/10.1016/j.cca.2019.03.1612.
[102] X. Liang, D. Gupta, J. Xie, E. Van Wonterghem, L. Van Hoecke, J. Hean, Z. Niu, M. Ghaeidamini, O.P.B. Wiklander, W. Zheng, R.J. Wiklander, R. He, D. R. Mamand, J. Bost, G. Zhou, H. Zhou, S. Roudi, H.Y. Estupiñán, J. Rädler, A. M. Zickler, A. Görgens, V.W.Q. Hou, R. Slovak, D.W. Hagey, O.G. de Jong, A. G. Uy, Y. Zong, I. Mäger, C.M. Perez, T.C. Roberts, D. Carter, P. Vader, E. K. Esbjörner, A. de Fougerolles, M.J.A. Wood, R.E. Vandenbroucke, J.Z. Nordin, S. EL Andaloussi, Engineering of extracellular vesicles for efficient intracellular delivery of multimodal therapeutics including genome editors, Nat. Commun. 16 (2025) 4028, https://doi.org/10.1038/s41467-025-59377-y.
[103] G. Rodgers, C. Tanner, G. Schulz, A. Migga, W. Kuo, C. Bikis, M. Scheel, V. Kurtcuoglu, T. Weitkamp, B. Müller, Virtual histology of an entire mouse brain from formalin fixation to paraffin embedding. Part 2: volumetric strain fields and local contrast changes, J. Neurosci. Methods 365 (2022) 109385, https://doi.org/10.1016/j.jneumeth.2021.109385.
[104] F. Hashim, M. El-Ridy, M. Nasr, Y. Abdallah, Preparation and characterization of niosomes containing ribavirin for liver targeting, Drug Deliv. 17 (5) (2010) 282–287, https://doi.org/10.3109/10717541003706257.
[105] E. Moazeni, K. Gilani, F. Sotoudegan, A. Pardakhty, A.R. Najafabadi, R. Ghalandari, M.R. Fazeli, H. Jamalifar, Formulation and in vitro evaluation of ciprofloxacin containing niosomes for pulmonary delivery, J. Microencapsul. 27 (7) (2010) 618–627, https://doi.org/10.3109/02652048.2010.506579.
[106] M.L. Briuglia, C. Rotella, A. McFarlane, D.A. Lamprou, Influence of cholesterol on liposome stability and drug release, Drug Deliv. Transl. Res. 5 (2015) 231–242, https://doi.org/10.1007/s13346-015-0220-8.
[107] A.R. Mohammed, N. Weston, A.G.A. Coombes, M. Fitzgerald, Y. Perrie, Liposome formulation of poorly water soluble drugs: optimisation of drug loading and ESEM analysis of stability, Int. J. Pharm. 285 (1–2) (2004) 23–34, https://doi.org/10.1016/j.ijpharm.2004.07.010.
[108] V.B. Junyaprasert, P. Singhsa, J. Suksiriworapong, D. Chantasart, Physicochemical properties and skin permeation of Span 60/Tween 60 niosomes of ellagic acid, Int. J. Pharm. 423 (2) (2012) 303–311, https://doi.org/10.1016/j.ijpharm.2011.11.032.
[109] D. Psimadas, P. Georgoulias, V. Valotassiou, G. Loudos, Molecular nanomedicine towards cancer: ^{111}In-Labeled Nanoin-licles, n. Pharm. Sci. 101 (7) (2012) 2271–2280, https://doi.org/10.1002/jps.23146.
[110] A. Akbarzadeh, R. Rezaei-Sadabady, S. Davaran, S.W. Joo, N. Zarghami, Y. Hanifehpour, M. Samiei, M. Kouhi, K. Nejati-Koshki, Liposome: classification, preparation, and applications, Nanoscale Res. Lett. 8 (2013) 102, https://doi.org/10.1186/1556-276X-8-102.
[111] S.M. Dizaj, F. Lotfipour, M. Barzegar-Jalali, M.H. Zarrintan, K. Adibkia, Box-Behnken experimental design for preparation and optimization of ciprofloxacin hydrochloride-loaded $CaCO_3$ nanoparticles, J. Drug Deliv. Sci. Technol. 29 (2015) 125–131, https://doi.org/10.1016/j.jddst.2015.06.015.
[112] L.M.P. Masson, A. Rosenthal, V.M.A. Calado, R. Deliza, L. Tashima, Effect of ultra-high pressure homogenization on viscosity and shear stress of fermented dairy beverage, LWT Food Sci. Technol. 44 (2) (2011) 495–501, https://doi.org/10.1016/j.lwt.2010.07.012.
[113] S. Kheradmandnia, E. Vasheghani-Farahani, M. Nosrati, F. Atyabi, Preparation and characterization of ketoprofen-loaded solid lipid nanoparticles made from beeswax and carnauba wax, Nanomed. Nanotechnol. Biol. Med. 6 (6) (2010) 753–759, https://doi.org/10.1016/j.nano.2010.06.003.
[114] H.A. Abo El-Enin, R.E. Mostafa, M.F. Ahmed, I.A. Naguib, M.A. Abdelgawad, M. M. Ghoneim, E.M. Abdou, Assessment of nasal-brain-targeting efficiency of new developed mucoadhesive emulsomes encapsulating an anti-migraine drug for effective treatment of one of the major psychiatric disorders symptoms, Pharmaceutics 14 (2) (2022) 410, https://doi.org/10.3390/pharmaceutics14020410.
[115] V.P. Torchilin, Recent advances with liposomes as pharmaceutical carriers, Nat. Rev. Drug Discov. 4 (2005) 145–160, https://doi.org/10.1038/nrd1632.
[116] M. Mokhtar, O.A. Sammour, M.A. Hammad, N.A. Megrab, Effect of some formulation parameters on flurbiprofen encapsulation and release rates of niosomes prepared from proniosomes, Int. J. Pharm. 361 (1–2) (2008) 104–111, https://doi.org/10.1016/j.ijpharm.2008.05.031.
[117] G. Abdelbary, Ocular ciprofloxacin hydrochloride mucoadhesive chitosan-coated liposomes, Pharmaceut. Dev. Technol. 16 (1) (2011) 44–56, https://doi.org/10.3109/10837450903479988.
[118] A.M. Al-Mahallawi, O.M. Khowessah, R.A. Shoukri, Nano-transfersomal ciprofloxacin loaded vesicles for non-invasive trans-tympanic ototopical delivery: In-vitro optimization, ex-vivo permeation studies, and in-vivo assessment, Int. J. Pharm. 472 (1–2) (2014) 304–314, https://doi.org/10.1016/j.ijpharm.2014.06.041.
[119] K. Moribe, K. Maruyama, M. Iwatsuru, Encapsulation characteristics of nystatin in liposomes: effects of cholesterol and polyethylene glycol derivatives, Int. J. Pharm. 188 (2) (1999) 193–202, https://doi.org/10.1016/S0378-5173(99)00222-7.
[120] M.S. El-Samaligy, N.N. Afifi, E.A. Mahmoud, Increasing bioavailability of silymarin using a buccal liposomal delivery system: preparation and experimental design investigation, Int. J. Pharm. 308 (1–2) (2006) 140–148, https://doi.org/10.1016/j.ijpharm.2005.11.006.
[121] F. Nowroozi, A. Almasi, J. Javidi, A. Haeri, S. Dadashzadeh, Effect of surfactant type, cholesterol content and various downsizing methods on the particle size of niosomes, Iran. J. Pharm. Res. (IJPR) 17 (Suppl 2) (2018) 1–11. PMCID: PMC6447874 PMID: 31011337.
[122] F. Kashani-Asadi-Jafari, A. Aftab, S. Ghaemmaghami, A machine learning framework for predicting entrapment efficiency in niosomal particles, Int. J. Pharm. 627 (2022) 122203, https://doi.org/10.1016/j.ijpharm.2022.122203.
[123] S. Bhattacharjee, DLS and zeta potential – what they are and what they are not? J. Contr. Release 235 (2016) 337–351, https://doi.org/10.1016/j.jconrel.2016.06.017.
[124] M.A. Bezerra, R.E. Santelli, E.P. Oliveira, L.S. Villar, L.A. Escaleira, Response surface methodology (RSM) as a tool for optimization in analytical chemistry, Talanta 76 (5) (2008) 965–977, https://doi.org/10.1016/j.talanta.2008.05.019.
[125] S.L.C. Ferreira, R.E. Bruns, H.S. Ferreira, G.D. Matos, J.M. David, G.C. Brandão, E. G.P. da Silva, L.A. Portugal, P.S. dos Reis, A.S. Souza, W.N.L. dos Santos, Box–Behnken design: an alternative for the optimization of analytical methods, Anal. Chim. Acta 597 (2) (2007) 179–186, https://doi.org/10.1016/j.aca.2007.07.011.
[126] D. Granato, V.M. de Araújo Calado, B. Jarvis, Observations on the use of statistical methods in Food Science and Technology, Food Res. Int. 55 (2014) 137–149, https://doi.org/10.1016/j.foodres.2013.10.024.
[127] C. Marianecci, D. Paolino, C. Celia, M. Fresta, M. Carafa, F. Alhaique, Non-ionic surfactant vesicles in pulmonary glucocorticoid delivery: characterization and interaction with human lung fibroblasts, J. Contr. Release 147 (1) (2010) 127–135, https://doi.org/10.1016/j.jconrel.2010.06.022.
[128] M. Hassanzadeganroudsari, A. Heydarinasab, A.A. Khiyavi, P. Chen, M. Soltani, In vitro investigation of anticancer efficacy of carboplatin-loaded PEGylated nanoliposome particles on brain cancer cell lines, J. Nanoparticle Res. 21 (2019) 124, https://doi.org/10.1007/s11051-019-4562-x.
[129] S. Wohlfart, S. Gelperina, J. Kreuter, Transport of drugs across the blood–brain barrier by nanoparticles, J. Contr. Release 161 (2) (2012) 264–273, https://doi.org/10.1016/j.jconrel.2011.08.017.
[130] C. Saraiva, C. Praça, R. Ferreira, T. Santos, L. Ferreira, L. Bernardino, Nanoparticle-mediated brain drug delivery: overcoming blood–brain barrier to treat neurodegenerative diseases, J. Contr. Release 235 (2016) 34–47, https://doi.org/10.1016/j.jconrel.2016.05.044.
[131] G. Tosi, L. Costantino, B. Ruozi, F. Forni, M.A. Vandelli, Polymeric nanoparticles for the drug delivery to the central nervous system, Expert Opin. Drug Deliv. 5 (2) (2008) 155–174, https://doi.org/10.1517/17425247.5.2.155.
[132] J. Pardeike, S. Weber, H.P. Zarfl, M. Pagitz, A. Zimmer, Itraconazole-loaded nanostructured lipid carriers (NLC) for pulmonary treatment of aspergillosis in falcons, Eur. J. Pharm. Biopharm. 108 (2016) 269–276, https://doi.org/10.1016/j.ejpb.2016.07.018.
[133] L. Wang, Q. Luo, T. Lin, R. Li, T. Zhu, K. Zhou, Z. Ji, J. Song, B. Jia, C. Zhang, W. Chen, G. Zhu, PEGylated nanostructured lipid carriers (PEG-NLC) as a novel drug delivery system for biochanin A, Drug Dev. Ind. Pharm. 41 (7) (2015) 1204–1212, https://doi.org/10.3109/03639045.2014.938082.
[134] M. Luangtana-Anan, S. Limmatvapirat, J. Nunthanid, R. Chalongsuk, K. Yamamoto, Polyethylene glycol on stability of chitosan microparticulate carrier for protein, AAPS PharmSciTech 11 (2010) 1376–1382, https://doi.org/10.1208/s12249-010-9512-y.
[135] M.L. Immordino, F. Dosio, L. Cattel, Stealth liposomes: review of the basic science, rationale, and clinical applications, existing and potential, Int. J. Nanomed. 1 (3) (2006) 297–315. PMCID: PMC2426795 PMID: 17717971.
[136] A. Guţoaia, L. Schuster, S. Margutti, S. Laufer, B. Schlosshauer, R. Krastev, D. Stoll, H. Hartmann, Fine-tuned PEGylation of chitosan to maintain optimal siRNA-nanoplex bioactivity, Carbohydr. Polym. 143 (2016) 25–34, https://doi.org/10.1016/j.carbpol.2016.01.010.
[137] R. Qi, Y.Z. Li, C. Chen, Y.N. Cao, M.M. Yu, L. Xu, B. He, X. Jie, W.W. Shen, Y. N. Wang, M.A.V. Dongen, G.Q. Liu, M.M.B. Holl, Q. Zhang, X. Ke, G5-PEG PAMAM dendrimer incorporating nanostructured lipid carriers enhance oral bioavailability and plasma lipid-lowering effect of probucol, J. Contr. Release 210 (2015) 160–168, https://doi.org/10.1016/j.jconrel.2015.05.281.
[138] R.M. Soliman, R.A. Abdel Salam, B.G. Eid, A. Khayyat, T. Neamatallah, M. K. Mesbah, G.M. Hadad, Stability study of thymoquinone, carvacrol and thymol using HPLC-UV and LC-ESI-MS, Acta Pharm. 70 (3) (2020) 325–342, https://doi.org/10.2478/acph-2020-0028.
[139] A. Bernkop-Schnürch, S. Dünnhaupt, Chitosan-based drug delivery systems, Eur. J. Pharm. Biopharm. 81 (3) (2012) 463–469, https://doi.org/10.1016/j.ejpb.2012.04.007.
[140] A. Pardakhty, J. Varshosaz, A. Rouholamini, In vitro study of polyoxyethylene alkyl ether niosomes for delivery of insulin, Int. J. Pharm. 328 (2) (2007) 130–141, https://doi.org/10.1016/j.ijpharm.2006.08.002.
[141] M.T. Heneka, D.T. Golenbock, E. Latz, Innate immunity in Alzheimer's disease, Nat. Immunol. 16 (2015) 229–236, https://doi.org/10.1038/ni.3102.

[142] H. Hampel, J. Hardy, K. Blennow, C. Chen, G. Perry, S.H. Kim, V.L. Villemagne, P. Aisen, M. Vendruscolo, T. Iwatsubo, C.L. Masters, M. Cho, L. Lannfelt, J. L. Cummings, A. Vergallo, The Amyloid-β pathway in alzheimer's disease, Mol. Psychiatr. 26 (2021) 5481–5503, https://doi.org/10.1038/s41380-021-01249-0.

[143] A. Baniasad, M.S. Baei, S.M. Tala-Tapeh, Chitosan-PEGylated niosomes and liposomes as biomacromolecule carriers for Alzheimer's disease treatment: galantamine drug delivery carrier, Mater. Chem. Phys. 352 (2026) 132003, https://doi.org/10.1016/j.matchemphys.2025.132003.

[144] G. Karmakar, P. Nahak, P. Guha, B. Roy, R.K. Nath, A.K. Panda, Role of PEG 2000 in the surface modification and physicochemical characteristics of pyrazinamide loaded nanostructured lipid carriers, J. Chem. Sci. 130 (2018) 42, https://doi.org/10.1007/s12039-018-1448-x.

[145] Y.C. Pyo, P. Tran, D.H. Kim, J.S. Park, Chitosan-coated nanostructured lipid carriers of fenofibrate with enhanced oral bioavailability and efficacy, Colloids Surf. B Biointerfaces 196 (2020) 111331, https://doi.org/10.1016/j.colsurfb.2020.111331.

[146] H. Li, Y. Tan, X. Cheng, Z. Zhang, J. Huang, S. Hui, L. Zhu, Y. Liu, D. Zhao, Z. Liu, W. Peng, Untargeted metabolomics analysis of the hippocampus and cerebral cortex identified the neuroprotective mechanisms of Bushen Tiansui formula in an $A\beta_{25\text{-}35}$-induced rat model of Alzheimer's disease, Front. Pharmacol. 13 (2022) 990307, https://doi.org/10.3389/fphar.2022.990307.

[147] F. Abbas, M.A. Eladl, M. El-Sherbiny, N. Abozied, A. Nabil, S.M. Mahmoud, H. I. Mokhtar, S.A. Zaitone, D. Ibrahim, Celastrol and thymoquinone alleviate aluminum chloride-induced neurotoxicity: behavioral psychomotor performance, neurotransmitter level, oxidative-inflammatory markers, and BDNF expression in rat brain, Biomed. Pharmacother. 151 (2022) 113072, https://doi.org/10.1016/j.biopha.2022.113072.

[148] P. Gangarde, S. Bhatt, R. Pujari, Assessment of neuroprotective potential of Cuscuta reflexa in aluminium chloride-induced experimental model of Alzheimer ' s disease: in vitro and in vivo studies, J. Trace Elem. Med. Biol. 88 (2025) 127612, https://doi.org/10.1016/j.jtemb.2025.127612.

[149] Y. Jasoria, M. Agrawal, S. Kumar, H. Chaudhary, K.K. Sahu, M. Singhal, S. Arora, P. Chandolia, S. Saha, K. Singh, S. Mahour, W. Akram, D. Jain, *In-vivo* evaluation of neuroprotective effect of Chinese plant *calendula officinalis* Linn. Flower Extract against Aluminium chloride-induced Alzheimer's in Wistar rats, Pharmacol. Res. Mod. Chin. Med. 12 (2024) 100458, https://doi.org/10.1016/j.prmcm.2024.100458.

[150] B.S. Thawkar, G. Kaur, Betanin combined with virgin coconut oil inhibits neuroinflammation in aluminum chloride-induced toxicity in rats by regulating NLRP3 inflammasome, J. Tradit. Complement. Med. 14 (3) (2024) 287–299, https://doi.org/10.1016/j.jtcme.2023.11.001.

[151] H. Zhang, L. Wang, B. Zhu, Y. Yang, C. Cai, X. Wang, L. Deng, B. He, Y. Cui, W. Zhou, A comparative study of the neuroprotective effects of dL-3-n-butylphthalide and edaravone dexborneol on cerebral ischemic stroke rats, Eur. J. Pharmacol. 951 (2023) 175801, https://doi.org/10.1016/j.ejphar.2023.175801.

[152] Z. Breijyeh, R. Karaman, Comprehensive review on Alzheimer's disease: causes and treatment, Molecules 25 (24) (2020) 5789, https://doi.org/10.3390/molecules25245789.

[153] A. Justin-Thenmozhi, M.D. Bharathi, R. Kiruthika, T. Manivasagam, A. Borah, M. M. Essa, Attenuation of aluminum chloride-induced neuroinflammation and caspase activation through the AKT/GSK-3β pathway by Hesperidin in Wistar rats, Neurotox. Res. 34 (2018) 463–476, https://doi.org/10.1007/s12640-018-9904-4.

[154] C. Ezzaki, A. Chaari, A. Al-Othman, Recent advances on chitosan-based nanoparticles for brain drug delivery, Polymers 17 (22) (2025) 3055, https://doi.org/10.3390/polym17223055.

[155] K.R. Gajbhiye, A. Pawar, K.R. Mahadik, V. Gajbhiye, PEGylated nanocarriers: a promising tool for targeted delivery to the brain, Colloids Surf. B Biointerfaces 187 (2020) 110770, https://doi.org/10.1016/j.colsurfb.2019.110770.

[156] I.N. Khan, S. Navaid, W. Waqar, D. Hussein, N. Ullah, M.U.A. Khan, Z. Hussain, A. Javed, Chitosan-Based polymeric nanoparticles as an efficient gene delivery System to cross blood brain barrier: in vitro and in vivo evaluations, Pharmaceuticals 17 (2) (2024) 169, https://doi.org/10.3390/ph17020169.

[157] U. Kochman, H. Sitka, J. Kuźniar, M. Czaja, P. Kozubek, J.A. Beszłej, J. Leszek, Targeted nanoparticles for drug delivery across the blood–brain barrier in early and late stages of alzheimer's disease: a review, Mol. Neurobiol. 63 (1) (2026) 75, https://doi.org/10.1007/s12035-025-05417-z.

[158] W.A. El-Kashak, A.F. Essa, M.F. Abdelhameed, Y.H. Ahmed, A.S. Abd Elkarim, M. M. Elghonemy, B.M.M. Ibrahim, A.H. Gaara, T.K. Mohamed, A.I. Elshamy, Unveiling the neuroprotective potential of Ipomoea carnea ethanol extract via the modulation of tau and β-secretase pathways in $AlCl_3$-induced memory impairment in rats in relation to its phytochemical profiling, Inflammopharmacology 33 (2025) 2043–2068, https://doi.org/10.1007/s10787-025-01687-0.